The Astrophysical Journal, 850:44 (17pp), 2017 November 20
https://doi.org/10.3847/1538-4357/aa9223

Resonant Absorption of Surface Sausage and Surface Kink Modes under Photospheric Conditions

Dae Jung Yu[1,2], Tom Van Doorsselaere[1], and Marcel Goossens[1]
[1] Centre for mathematical Plasma Astrophysics, Department of Mathematics, KU Leuven Celestijnenlaan 200B bus 2400, B-3001 Leuven, Belgium
djyu79@gmail.com, tom.vandoorsselaere@kuleuven.be, marcel.goossens@kuleuven.be
[2] School of Space Research, Kyung Hee University, Yongin 17104, Korea
Received 2017 July 5; revised 2017 September 20; accepted 2017 October 5; published 2017 November 15

Abstract

We study the effect of resonant absorption of surface sausage and surface kink modes under photospheric conditions where the slow surface sausage modes undergo resonant damping in the slow continuum and the surface kink modes in the slow and Alfvén continua at the transitional layers. We use recently derived analytical formulas to obtain the damping rate (time). By considering linear density and linear pressure profiles for the transitional layers, we show that resonant absorption in the slow continuum could be an efficient mechanism for the wave damping of the slow surface sausage and slow surface kink modes while the damping rate of the slow surface kink mode in the Alfvén continuum is weak. It is also found that the resonant damping of the fast surface kink mode is much stronger than that of the slow surface kink mode, showing a similar efficiency as under coronal conditions. It is worth noting that the slow body sausage and kink modes can also resonantly damp in the slow continuum for those linear profiles.

Key words: magnetohydrodynamics (MHD) – Sun: activity – Sun: oscillations – Sun: photosphere

1. Introduction

The observed magnetohydrodynamic (MHD) waves in the solar atmosphere are considered to be crucial ingredients for the coronal heating problem (e.g., Ionson 1978; Heyvaerts & Priest 1983; Hollweg 1988; Poedts et al. 1989, 1990; Ofman & Davila 1995; Roberts 2000; Goossens et al. 2011; Okamoto et al. 2015; Antolin et al. 2017; Cally 2017). The oscillation and rapid damping of MHD waves have made it possible to infer the physical parameters of the environment, as seismological tools. Resonant absorption has been treated as a most plausible mechanism for the rapid damping of the MHD wave oscillations and used as coronal seismology (e.g., Goossens et al. 2002; Arregui et al. 2007; Goossens et al. 2008; McEwan et al. 2008; Wang et al. 2009; Wang 2011; Goossens et al. 2012; Moreels & Van Doorsselaere 2013; Soler et al. 2014; Moreels et al. 2015a, 2015b; Wang 2016; Raes et al. 2017).

Since the energy source of the high temperature of the corona is believed to be from the convection zone below the surface of the Sun, the dynamics of MHD waves in the photosphere or chromosphere is of significant interest (see, e.g., Jess et al. 2015; Jess & Verth 2016), where sausage, kink, and torsional Alfvén waves have mainly been investigated.

Whereas resonant absorption under coronal conditions has been extensively studied (e.g., Ionson 1978; Poedts et al. 1989; Ofman & Davila 1995; Goossens et al. 2002; Ruderman & Roberts 2002; Aschwanden et al. 2003; Terradas et al. 2006a, 2006b; Ruderman and Erdélyi 2009; Pascoe et al. 2010; Goossens et al. 2011; Soler et al. 2013; Okamoto et al. 2015; Yu & Van Doorsselaere 2016; Karampelas et al. 2017; Scherrer & McKenzie 2017), its role in the lower solar atmosphere is not well understood yet (Hollweg 1988; Lou 1990; Rosenthal 1990, 1992; Stenuit et al. 1993; Keppens et al. 1994; Bogdan et al. 1996; Keppens 1996; Ruderman 2009; Giagkiozis et al. 2016).

In the lower atmosphere, alongside the Alfvén resonance, the slow (cusp) resonance can also be an important mechanism for wave energy conversion and transport. It has generally been anticipated that the effect of resonant absorption in the slow (cusp) continuum is feeble compared to that of resonant absorption in the Alfvén continuum (see, e.g., Soler et al. 2009), which, as we recently showed in Yu et al. (2017), is not true for the photospheric (magnetic pore) environment. The resonant absorption mechanism may cause efficient damping of sausage modes in the photosphere, in addition to other damping effects like thermal conduction, compressive viscosity, area divergence, optically thin radiation, and so on (e.g., De Moortel & Hood 2003, 2004; Khodachenko et al. 2004; Mandal et al. 2016).

Although we showed that the role of resonant absorption of the slow surface sausage (sss) mode in the slow continuum is important for the wave damping, the model for the transitional layers was a linear cusp speed profile, which is a simple one. In this paper, we put the model for the transitional layer in a more general case: linear density and linear pressure (or squared magnetic field) profiles and study resonant absorption of both the surface sausage and surface kink waves under magnetic pore conditions motivated by the recent observation of the slow sausage ($m = 0$) and kink ($m = 1$) modes simultaneously excited in a sunspot by Jess et al. (2017). We concentrate on the damping rate and damping time in this paper.

We organize the paper as follows. In Section 2, we obtain the dispersion relation of surface sausage and surface kink modes under magnetic pore conditions for a plasma, which is homogeneous inside and outside the pore. In Section 3, we derive the damping rate for the slow surface waves by considering a thin transitional layer between inner and outer regions of the pore by using the connection formulae. In Section 4, we introduce the model configuration for the transitional layer. The results are shown in Section 5. We conclude the paper in Section 6.

2. Dispersion Relation

2.1. Dispersion Relation

In our previous paper (Yu et al. 2017), we showed the dispersion relation for the fast and slow sausage modes under magnetic pore conditions by considering a uniform axisymmetric cylinder. In this paper, we also consider the surface kink modes. We assume that the inside magnetic field B_i and the outside magnetic field B_e are parallel to the axis ($\hat{z}$) and that no steady flow is present. Then the pressures inside and outside the flux tube satisfy the pressure balance equation

$$p_e + \frac{B_e^2}{2\mu_0} = p_i + \frac{B_i^2}{2\mu_0}, \tag{1}$$

where μ_0 is the magnetic permeability and p is the plasma pressure. The subscript $i(e)$ denotes the inner (outer) region of the flux tube.

We start from linearized ideal MHD equations by assuming $\exp(i(k_{zz} + m\phi - \omega t))$ dependence, where k_z is the longitudinal wavenumber, m is the azimuthal wavenumber, and ω is the angular frequency of the wave. Here we consider no transitional layer and different physical values for the inside and outside of the flux tube boundary at $r = R$. The density ρ is assumed to be ρ_i inside and ρ_e outside of the boundary and the same is applied for B and p. The dispersion relation is then obtained by the condition of continuity at the boundary ($r = R$) (e.g., Edwin & Roberts 1983; Sakurai et al. 1991; Goossens et al. 1992; Yu et al. 2017):

$$[P] = P_e - P_i = 0, \tag{2}$$

$$[\xi_r] = \frac{1}{\rho_e(\omega^2 - \omega_{Ae}^2)}\frac{dP_e}{dr} - \frac{1}{\rho_i(\omega^2 - \omega_{Ai}^2)}\frac{dP_i}{dr} = 0, \tag{3}$$

where P is the total pressure perturbation and ξ_r is the radial component of the Lagrangian displacement.

For the inner and outer homogeneous regions of the flux tube, the equations for P and ξ_r are satisfied by Bessel functions where the argument is the radial component.

For the surface wave modes, Equations (2) and (3) are combined to yield (e.g., Edwin & Roberts 1983; Yu et al. 2017)

$$\frac{A_e k_e K_m'(k_e R)}{\rho_e(\omega^2 - \omega_{Ae}^2)} - \frac{A_i k_i I_m'(k_i R)}{\rho_i(\omega^2 - \omega_{Ai}^2)} = 0, \tag{4}$$

where the prime denotes the derivative with respect to the entire argument, I_m and K_m are modified Bessel functions of first and second kinds, respectively, $A_{i,e}$ is the matching coefficient, and k_i and k_e are given by

$$k_i^2 = -\frac{(\omega^2 - \omega_{si}^2)(\omega^2 - \omega_{Ai}^2)}{(v_{si}^2 + v_{Ai}^2)(\omega^2 - \omega_{Ci}^2)}, \tag{5}$$

$$k_e^2 = -\frac{(\omega^2 - \omega_{se}^2)(\omega^2 - \omega_{Ae}^2)}{(v_{se}^2 + v_{Ae}^2)(\omega^2 - \omega_{Ce}^2)}, \tag{6}$$

where $\omega_C = k_z v_C$ is the cusp frequency, $v_C = \sqrt{v_s^2 v_A^2/(v_s^2 + v_A^2)}$ is the cusp speed, $\omega_s = k_z v_s$, $v_s = \sqrt{\gamma p/\rho}$ is the sound speed, $v_A = B/\sqrt{\mu_0 \rho}$ is the Alfvén speed, γ is the adiabatic index, and ρ is the density.

From the continuity of total pressure ($A_i I_m = A_e K_m$), we obtain the dispersion relation $D_m = 0$ for azimuthal wavenumber m:

$$D_m = \rho_i(\omega^2 - \omega_{Ai}^2) - \rho_e(\omega^2 - \omega_{Ae}^2)\left(\frac{k_i}{k_e}\right)Q_m = 0, \tag{7}$$

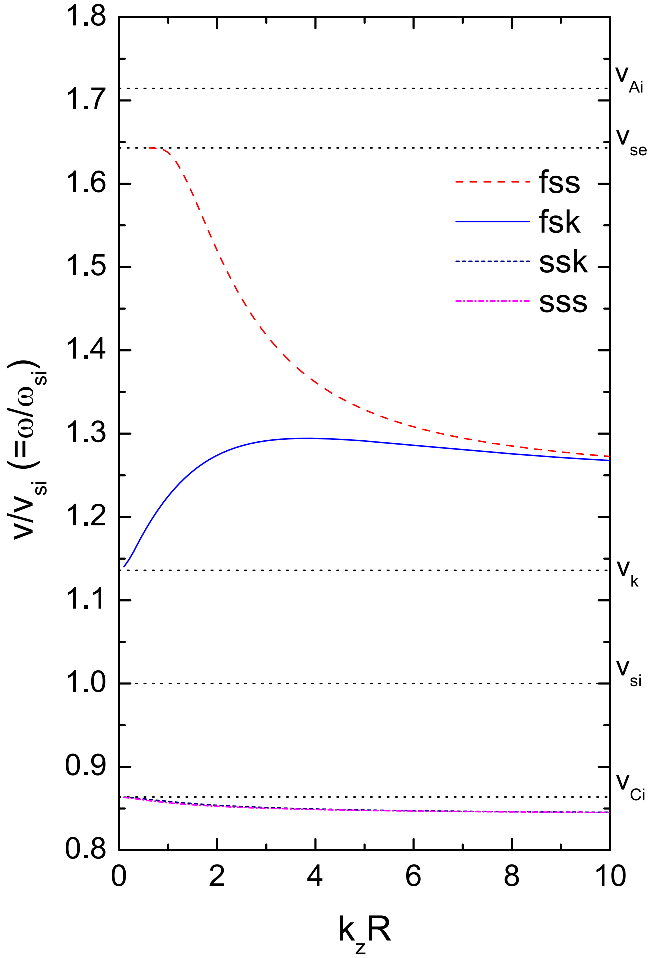

Figure 1. Phase speed $v/v_{si}(=\omega_r/\omega_{si})$ as a function of k_zR for a fast surface sausage mode (fss), a fast surface kink mode (fsk), a slow surface kink mode (ssk), and a slow surface sausage mode (sss) under the magnetic pore condition when $v_{Ae} = 0$ km s^{-1}, $v_{Ai} = 12$ km s^{-1}, $v_{se} = 11.5$ km s^{-1}, $v_{si} = 7$ km s^{-1}, $v_{Ce} = 0$ km s^{-1}, $v_{Ci} \approx 6.05$ km s^{-1} ($\approx 0.86 v_{si}$), $\beta_i = (2/\gamma)(v_{si}/v_{Ai})^2 \approx 0.41$, and $\beta_e = (2/\gamma)(v_{se}/v_{Ae})^2 = \infty$. The two slow surface modes are indistinguishable in the figure. All quantities are normalized by v_{si}.

where

$$Q_m = \frac{I_m'(k_i R) K_m(k_e R)}{I_m(k_i R) K_m'(k_e R)}. \tag{8}$$

We are concerned with the sausage and kink modes ($m = 0, 1$) in this paper. Equation (7) can be rewritten as

$$\omega^2 = \frac{\rho_i \omega_{Ai}^2 - \rho_e \omega_{Ae}^2 \left(\frac{k_i}{k_e}\right) Q_m}{\rho_i - \rho_e\left(\frac{k_i}{k_e}\right) Q_m} \text{ (for } m = 0,\ 1). \tag{9}$$

The rhs of Equation (9) also includes ω in k_i, k_e, and Q_m; therefore, this equation needs to be numerically solved (see, e.g., Edwin & Roberts 1983; Yu et al. 2017).

We use the same parameter values as in Yu et al. (2017) for the magnetic pore conditions (see also Grant et al. 2015). We plot surface wave eigenmodes for $m = 0,1$ in Figure 1: fast surface sausage mode (fss), fast surface kink mode (fsk), slow surface kink mode (ssk), and sss mode where $v_{Ae} = 0$ km s^{-1}, $v_{Ai} = 12$ km s^{-1}, $v_{se} = 11.5$ km s^{-1}, $v_{si} = 7$ km s^{-1}, $v_{Ce} = 0$ km s^{-1}, and $v_{Ci} \approx 6.05$ km s^{-1} ($\approx 0.86 v_{si}$). We distinguish between fast and slow modes by their phase speed: the fast mode lies above the kink speed $v_k = \sqrt{(\rho_i v_{Ai}^2 + \rho_e v_{Ae}^2)/(\rho_i + \rho_e)}$ and the slow mode lies below v_{Ci}. Another characteristic is the behavior of the ratio of the longitudinal to the transverse components of the Lagrangian displacement $\tilde{\xi} = \xi_{\parallel}/\xi_{\perp}$ such that for the fast modes $\tilde{\xi} \lesssim 1$ and for the slow modes $\tilde{\xi} > 1$ (see, e.g., Moreels & Van Doorsselaere 2013). For the slow modes, the longitudinal motion is dominant.

It follows from the figure that the slow surface sausage and kink modes are in the cusp frequency range ($v_{Ce} < v_{\rm sss,ssk} \leqslant v_{Ci}$), while both fast and surface kink modes are in the range of $v_{Ae} < v_{\rm fsk,ssk} < v_{Ai}$. This implies that when the discontinuity is replaced by continuous variation in the transitional layers, the slow surface sausage mode and slow surface kink mode lie in the slow (cusp) continuum and as a result damp resonantly in the resonant layer. The same phenomenon occurs for the surface kink modes (fsk, ssk) in the Alfvén continuum. There also exist multiple body modes for sausage and kink waves in the range of $v_{Ci} < v < v_{si}$, which are not shown in the figure. Since our concern is on the resonant absorption of the surface waves, we do not consider resonant absorption of the body modes here.

2.2. Approximate Dispersion Relation for the Slow Surface Kink Mode at $\omega \approx \omega_{Ci}$

For $k_z R \ll 1$ and $\omega \approx \omega_{Ci}$, we can assume $\omega^2 = \omega_{Ci}^2 - \alpha$, then the condition $D_1 = 0$ (Equation (7)) leads with the aid of Equation (67) (dropping all higher order terms of $k_{i\rm R}$ and $k_{e\rm R}$) to

$$\rho_i(\omega_{Ci}^2 - \omega_{Ai}^2) + \rho_e(\omega_{Ci}^2 - \omega_{Ae}^2)\left(1 + \frac{k_i^2 R^2}{4}\right) = 0. \tag{10}$$

In this limit, we obtain

$$\begin{aligned} k_i^2 &\approx \frac{k_z^2}{\alpha}\frac{(\omega_{Ci}^2 - \omega_{si}^2)(\omega_{Ci}^2 - \omega_{Ai}^2)}{(\omega_{si}^2 + \omega_{Ai}^2)} \\ &= \frac{k_z^2}{\alpha}\frac{\omega_{Ci}^6}{\omega_{si}^2\omega_{Ai}^2}, \end{aligned} \tag{11}$$

where we have used the relations $(\omega_{Ci}^2 - \omega_{si}^2) = -(\omega_{si}^2\omega_{Ci}^2)/\omega_{Ai}^2$ and $(\omega_{Ci}^2 - \omega_{Ai}^2) = -(\omega_{Ai}^2\omega_{Ci}^2)/\omega_{si}^2$.

Using Equations (10) and (11), we obtain an expression for α as

$$\alpha = \frac{\chi}{4}\frac{\omega_{Ci}^6(\omega_{Ci}^2 - \omega_{Ae}^2)}{\omega_{Ci}^2\omega_{Ai}^4 - \chi\omega_{si}^2\omega_{Ai}^2(\omega_{Ci}^2 - \omega_{Ae}^2)}k_z^2 R^2, \tag{12}$$

where $\chi = \rho_e/\rho_i = (2v_{si}^2 + \gamma v_{Ai}^2)/(2v_{se}^2 + \gamma v_{Ae}^2)$.

In Figure 2, we compare this formula, Equation (12), with the numerical result under magnetic pore conditions. As shown in the figure, Equation (12) is accurate for $k_z R \ll 1$.

The formula for k_i^2 then reduces to

$$\begin{aligned} k_i^2 &= \frac{k_z^2}{\alpha}\frac{\omega_{Ci}^6}{\omega_{si}^2\omega_{Ai}^2} \\ &= \frac{4}{\chi}\frac{\omega_{Ci}^2\omega_{Ai}^4 - \chi\omega_{si}^2\omega_{Ai}^2(\omega_{Ci}^2 - \omega_{Ae}^2)}{\omega_{si}^2\omega_{Ai}^2(\omega_{Ci}^2 - \omega_{Ae}^2)R^2} \\ &= \frac{4}{R^2}\left(\frac{\omega_{Ci}^2\omega_{Ai}^2}{\chi\omega_{si}^2(\omega_{Ci}^2 - \omega_{Ae}^2)} - 1\right). \end{aligned} \tag{13}$$

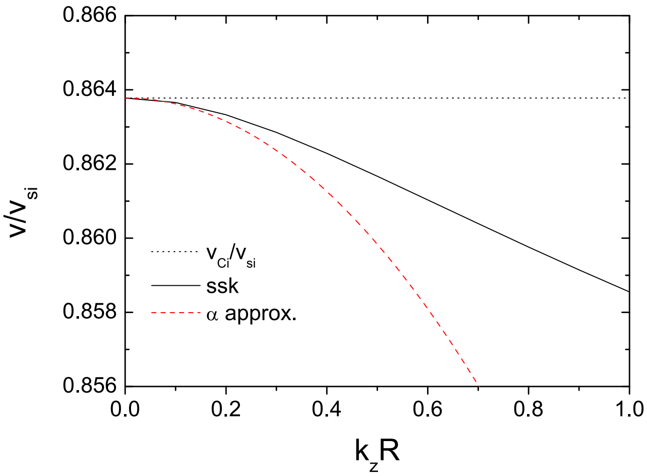

Figure 2. Dispersion curve as a function of $k_z R$ under magnetic pore conditions when $v_{Ae} = 0$ km s^{-1}, $v_{Ai} = 12$ km s^{-1}, $v_{se} = 11.5$ km s^{-1}, $v_{si} = 7$ km s^{-1}, $v_{Ce} = 0$ km s^{-1}, and $v_{Ci} \approx 6.05$ km s^{-1}. We compare the numerical result, Equation (9), with the analytical formula, Equation (12).

For k_e, we have

$$k_e \approx k_z\sqrt{-\frac{(\omega_{Ci}^2 - \omega_{se}^2)(\omega_{Ci}^2 - \omega_{Ae}^2)}{(\omega_{se}^2 + \omega_{Ae}^2)(\omega_{Ci}^2 - \omega_{Ce}^2)}} = k_z n_z. \tag{14}$$

We use these formulas when we derive an analytical damping rate in the long wavelength limit.

3. Resonant Absorption Due to the Transitional Layers

Considering transitional layers, which have a continuous variation from the inside to the outside of the flux tube, we need to solve, for example, a second-order ordinary differential equation for ξ_r (e.g., Sakurai et al. 1991; Goossens et al. 1992; Giagkiozis et al. 2016; Yu et al. 2017):

$$\frac{d}{dr}\left[\frac{D}{rC}\frac{d(r\xi_r)}{dr}\right] + \rho(\omega^2 - \omega_A^2)\xi_r = 0, \tag{15}$$

where

$$D = \rho(\omega^2 - \omega_A^2)(\omega^2 - \omega_C^2)(v_s^2 + v_A^2), \tag{16}$$

$$C = \omega^4 - (v_s^2 + v_A^2)(\omega^2 - \omega_C^2)\left(\frac{m^2}{r} + k_z^2\right). \tag{17}$$

This differential equation has singularities at $\omega = \omega_C(r)$ and $\omega = \omega_A(r)$ where resonant absorption can occur, resulting in damping of the wave amplitude. Due to the presence of the transitional layer, the value of $\omega_C(v_C)$ changes continuously from $\omega_{Ci}(v_{Ci})$ to $\omega_{Ce}(v_{Ce})$ and that of $\omega_A(v_A)$ from $\omega_{Ai}(v_{Ai})$ to $\omega_{Ae}(v_{Ae})$. These regimes are called slow (cusp) and Alfvén continua, respectively. For the magnetic pore conditions, we obtain the relation $0 = v_{Ce} = v_{Ae} < v_{Ci} < v_{si} < v_{se} < v_{Ai}$ (see Figures 1 and 3) and no modes exist for $v > v_{se}$. The slow surface sausage mode lies in the range of $0 = v_{Ce} < v_{\rm sss} < v_{Ci}$, so it can undergo resonant absorption in the slow continuum. This also applies to the slow surface kink mode since it is in the same range of the slow resonance. For the Alfvén resonance, both the fast and slow surface kink modes lie in the range of $0 = v_{Ae} < v_{\rm fsk,ssk} < v_{Ai}$, so two surface kink modes can undergo resonant absorption in the

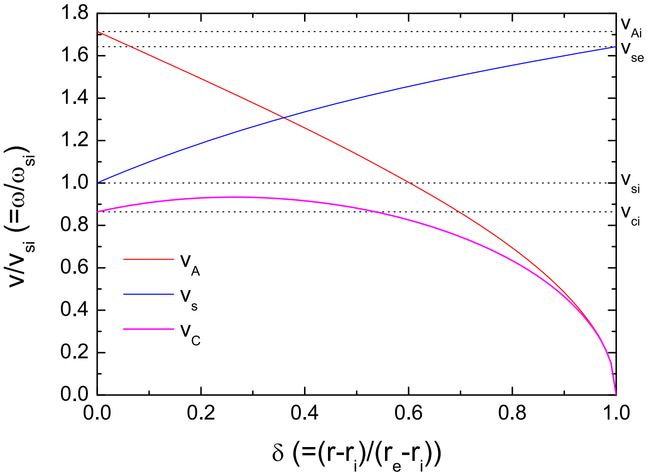

Figure 3. Profiles for v_s, v_A, and v_C as a function of δ in the nonuniform (transitional) layer under magnetic pore conditions when $v_{Ae} = 0$ km s^{-1}, $v_{Ai} = 12$ km s^{-1}, $v_{se} = 11.5$ km s^{-1}, $v_{si} = 7$ km s^{-1}, $v_{Ce} = 0$ km s^{-1}, and $v_{Ci} \approx 6.05$ km s^{-1}. When $v_{Ci} < v < v_{Cm}$ the slow body sausage modes can resonantly damp in the slow continuum where v_{Cm} is the maximum value of v_C. When $v < v_{Ci}$ the slow surface sausage mode can resonantly damp in the slow continuum. The slow surface kink mode may resonantly damp both in the slow continuum and in the Alfvén continuum while the fast surface kink mode undergoes resonant absorption in the Alfvén continuum. There is no resonant absorption for the sausage modes in the Alfvén continuum when the external magnetic field is along the tube axis (no azimuthal component) as considered in this paper.

Alfvén continuum. There is no resonant absorption of sausage modes in the Alfvén continuum when the magnetic field is along the flux tube. The resonant absorption of the sausage mode in the Alfvén continuum was studied by Giagkiozis et al. (2016) by considering weakly twisted magnetic flux tubes.

We are interested in the damping rate for thin transitional layers. Therefore, instead of numerically solving Equation (15), we use a connection formula (e.g., Sakurai et al. 1991; Goossens et al. 1992; Soler et al. 2009; Giagkiozis et al. 2016; Yu et al. 2017), which is demonstrated in the following sections.

We start with a general derivation with $v_{Ae} \neq 0$ and later focus on the magnetic pore conditions with $v_{Ae} = 0$.

3.1. Connection Formula

As shown in Section 2, the eigenfrequency of the slow surface sausage mode is in the slow resonance range of $\omega_r(v_{\rm sss}) < \omega_{Ci}(v_{Ci})$ and that of kink modes in the Alfvén resonance range of $\omega_{Ae}(v_{Ae}) < \omega_r(v_{\rm fsk,ssk}) < \omega_{Ai}(v_{Ai})$. Therefore, these modes will undergo resonant damping in the transitional layers. When there is resonant absorption (damping), an imaginary term is included in the original dispersion relation as follows (e.g., Sakurai et al. 1991; Goossens et al. 1992).

Instead of the discontinuity at $r = R$, we assume a continuous variation of ρ from ρ_i to ρ_e in a nonuniform (transitional) layer $[R - l/2, R + l/2]$ and similarly for p and B. The thickness of the nonuniform layer is set to l. A fully nonuniform flux tube corresponds to $l = 2R$. By using the thin boundary approximation, we can use the analytic solutions for P and ξ_r in the intervals $[0, R - l/2]$ and $[R + l/2, \infty[$, avoiding numerical integration of Equation (15). The connection formula for P is, without reference to the kind of resonance, given as

$$[P] = 0, \tag{18}$$

which is the same as for no resonance (Equation (2)). While the connection formula for ξ_r is given for the slow resonance as

$$[\xi_r] = -i\pi\frac{k_z^2}{\rho_c|\triangle_c|}\left(\frac{v_{sc}^2}{v_{sc}^2 + v_{Ac}^2}\right)^2 P_c, \tag{19}$$

where subscript c denotes the position of the slow resonance ($r = r_c$) and $\triangle_c = d(\omega^2 - \omega_C^2)/dr|_{r=r_c}$, and for the Alfvén resonance

$$[\xi_r] = -i\pi\frac{m^2}{\rho_A|\triangle_A|r_A^2}P_A\ , \tag{20}$$

where subscript A denotes the position of the Alfvén resonance ($r = r_A$) and $\triangle_A = d(\omega^2 - \omega_A^2)/dr|_{r=r_A}$.

From Equations (3), (19), and (20), we obtain

$$\frac{P_e'}{\rho_e(\omega^2 - \omega_{Ae}^2)} - \frac{P_i'}{\rho_i(\omega^2 - \omega_{Ai}^2)} = -i\pi\frac{k_z^2}{\rho_c|\triangle_c|}\left(\frac{v_{sc}^2}{v_{sc}^2 + v_{Ac}^2}\right)^2 P_c, \tag{21}$$

and

$$\frac{P_e'}{\rho_e(\omega^2 - \omega_{Ae}^2)} - \frac{P_i'}{\rho_i(\omega^2 - \omega_{Ai}^2)} = -i\pi\frac{m^2}{\rho_A|\triangle_A|r_A^2}P_A. \tag{22}$$

3.2. Analytical Solution for the Damping Rate of the Slow Surface Modes of Sausage and Kink Waves in the Slow Continuum

In our previous paper (Yu et al. 2017), we have developed an analytical formula for the damping rate of the slow mode in the slow continuum. Here we introduce again the procedure for obtaining the damping rate. For the surface mode, Equation (21) can be reduced to

$$\frac{A_e k_e K_m'(k_e R)}{\rho_e(\omega^2 - \omega_{Ae}^2)} - \frac{A_i k_i I_m'(k_i R)}{\rho_i(\omega^2 - \omega_{Ai}^2)} + \frac{i\pi k_z^2}{\rho_c|\triangle_c|}\left(\frac{v_{sc}^2}{v_{sc}^2 + v_{Ac}^2}\right)^2 A_e K_m(k_e R) = 0, \tag{23}$$

where we have used the continuity of P ($P_i = P_e = P_c$) and $A_{i,e,c}$ is the matching coefficient.

As before, for the discontinuous case, we can eliminate the coefficients A_i, A_e to arrive at the dispersion relation. The dispersion function D_m has a real and an imaginary part: $D_m = D_{mr} + iD_{mi}$. Eliminating the matching coefficients by using the continuity of the total pressure, we have the dispersion relation for $D_m = 0$

$$\rho_i(\omega^2 - \omega_{Ai}^2) - \rho_e(\omega^2 - \omega_{Ae}^2)\frac{k_i}{k_e}Q_m + \frac{i\pi k_z^2}{\rho_c|\triangle_c|}\left(\frac{v_{sc}^2}{v_{sc}^2 + v_{Ac}^2}\right)^2 \rho_i\rho_e(\omega^2 - \omega_{Ai}^2) \times(\omega^2 - \omega_{Ae}^2)\frac{G_m}{k_e} = 0, \tag{24}$$

where

$$G_m = \frac{K_m(k_e R)}{K_m'(k_e R)}. \tag{25}$$

We define D_{mi} as

$$D_{mi} = \frac{\pi\rho_i\rho_e k_z^2}{k_e\rho_c|\Delta_c|}\left(\frac{v_{sc}^2}{v_{sc}^2 + v_{Ac}^2}\right)^2(\omega^2 - \omega_{Ai}^2)(\omega^2 - \omega_{Ae}^2)G_m, \tag{26}$$

and D_{mr} as

$$D_{mr} = \rho_i(\omega^2 - \omega_{Ai}^2) - \rho_e(\omega^2 - \omega_{Ae}^2)\left(\frac{k_i}{k_e}\right)Q_m, \tag{27}$$

which is the same as Equation (7).

Due to resonant damping, the wave frequency has a real and an imaginary part: $\omega = \omega_r + i\gamma_m$. The imaginary part γ_m can be obtained by $\gamma_m = -D_{mi}/(\partial D_{mr}/\partial\omega)|_{\omega=\omega_r}$ (e.g., Krall & Trivelpiece 1973; Goossens et al. 1992) by assuming $|\gamma_m| \ll \omega_r$.

The analytical formula for γ_m (see Appendix B) in the slow (cusp) continuum is given as

$$\gamma_{cm} = -\frac{\frac{\pi\rho_e k_z^2}{k_e\rho_c\,|\Delta_c|}\left(\frac{v_{sc}^2}{v_{sc}^2 + v_{Ac}^2}\right)^2(\omega_r^2 - \omega_{Ai}^2)(\omega_r^2 - \omega_{Ae}^2)G_m}{2\omega_r\left[1 - \chi\left(\frac{k_i}{k_e}\right)Q_m\right] - \omega_r\chi T_m}, \tag{28}$$

where

$$T_m = \omega_r^2(\omega_r^2 - \omega_{Ae}^2)\left(\frac{k_i}{k_e}\right)\left\{\frac{(\omega_r^2 - 2\omega_{Ci}^2)[Q_m + k_i R P_m]}{(\omega_r^2 - \omega_{si}^2)(\omega_r^2 - \omega_{Ai}^2)(\omega_r^2 - \omega_{Ci}^2)} - \frac{(\omega_r^2 - 2\omega_{Ce}^2)[Q_m - k_e R S_m]}{(\omega_r^2 - \omega_{se}^2)(\omega_r^2 - \omega_{Ae}^2)(\omega_r^2 - \omega_{Ce}^2)}\right\}, \tag{29}$$

$$P_m = \left(\frac{I_m''}{I_m} - \frac{I_m'^2}{I_0^2}\right)\frac{K_m}{K_m'}, \tag{30}$$

$$S_m = \left(1 - \frac{K_m'' K_m}{K_m'^2}\right)\frac{I_m'}{I_m}. \tag{31}$$

For the sausage ($m = 0$) and kink ($m = 1$) modes in the slow continuum, we obtain

$$\gamma_{c0} = -\frac{\pi\rho_e k_z^2}{k_e\rho_c|\Delta_c|}\left(\frac{v_{sc}^2}{v_{sc}^2 + v_{Ac}^2}\right)^2\frac{(\omega_r^2 - \omega_{Ai}^2)(\omega_r^2 - \omega_{Ae}^2)G_0}{2\omega_r\left[1 - \chi\left(\frac{k_i}{k_e}\right)Q_0\right] - \omega_r\chi T_0}, \tag{32}$$

and

$$\gamma_{c1} = -\frac{\pi\rho_e k_z^2}{k_e\rho_c|\Delta_c|}\left(\frac{v_{sc}^2}{v_{sc}^2 + v_{Ac}^2}\right)^2\frac{(\omega_r^2 - \omega_{Ai}^2)(\omega_r^2 - \omega_{Ae}^2)G_1}{2\omega_r\left[1 - \chi\left(\frac{k_i}{k_e}\right)Q_1\right] - \omega_r\chi T_1}. \tag{33}$$

A nonzero value of v_{Ae} has opposite effects on γ, since it decreases the value of $\omega_{Ci}^2 - \omega_{Ae}^2$ in the numerator and decreases the value of $|\Delta_c|$ in the denominator, which may increase or decrease the damping rate depending on the variation of the two factors. This equally applies to the damping in the Alfvén resonance.

3.3. Long Wavelength Limit ($m = 0, 1$)

We derived previously an analytical expression for the damping rate of the slow surface sausage mode in the slow continuum in the long wavelength limit (Yu et al. 2017). Here we describe the result briefly. In the limit $k_i R(k_e R) \ll 1$, we obtain

$$\gamma_{c0} = -\frac{\pi\rho_i\rho_e k_z^2 R}{\rho_c|\Delta_c|}\left(\frac{v_{sc}^2}{v_{sc}^2 + v_{Ac}^2}\right)^2 \times \frac{(\omega_r^2 - \omega_{Ai}^2)(\omega_r^2 - \omega_{Ae}^2)\ln(k_e R)}{2\omega_r\left\{\rho_i - \frac{\rho_e k_i^2 R^2}{2}\ln(k_e R)\right\} - \rho_e\omega_r T_0}, \tag{34}$$

where

$$T_0 = \omega_r^2(\omega_r^2 - \omega_{Ae}^2)\left\{\frac{3}{16}\frac{(\omega_r^2 - 2\omega_{ci}^2)k_i^4 R^4\ln(k_e R)}{(\omega_r^2 - \omega_{si}^2)(\omega_r^2 - \omega_{Ai}^2)(\omega_r^2 - \omega_{Ci}^2)} + \frac{(\omega_r^2 - 2\omega_{Ce}^2)k_i^2 R^2}{2(\omega_r^2 - \omega_{se}^2)(\omega_r^2 - \omega_{Ae}^2)(\omega_r^2 - \omega_{Ce}^2)}\right\}. \tag{35}$$

When $\omega_r \approx \omega_{Ci}$ ($k_z R \ll 1$) Equation (34) becomes

$$\gamma_{c0} = \frac{2\pi\chi^3}{3|\Delta_c|R}\frac{\omega_{Ci}^5\omega_{si}^2(\omega_{Ci}^2 - \omega_{Ae}^2)^3}{\omega_{Ai}^{10}}(k_z R)^4\ln^3(k_z R), \tag{36}$$

where we have used $\ln(k_e R) \approx \ln(k_z R)$.

Under photospheric (magnetic pore) conditions, where $\omega_{Ae}(\omega_{Ce}) \simeq 0$, Equation (36) can be reduced to

$$\gamma_{c0} = \frac{2\pi\chi^3}{3|\Delta_c|R}\frac{\omega_{Ci}^{11}\omega_{si}^2}{\omega_{Ai}^{10}}(k_z R)^4\ln^3(k_z R). \tag{37}$$

Likewise, using the approximations for G_1, Q_1, and T_1 used in Section 3.5, we find for Equation (33) under magnetic pore conditions

$$\gamma_{c1} \approx -\frac{\pi}{8|\Delta_c|R}\frac{\omega_{Ci}^7 k_z^4 R^4}{\omega_{si}^4}\frac{\omega_{\mathbf{Ci}}^4}{\omega_{Ai}^4}\left(\frac{\omega_{Ai}^2}{\chi\omega_{si}^2} - 1\right)^{-2} = -\frac{\pi}{8|\Delta_c|R}\frac{\chi^2\omega_{Ci}^{11}k_z^4 R^4}{\omega_{Ai}^4(\omega_{Ai}^2 - \chi\omega_{si}^2)^2}. \tag{38}$$

For comparison of Equations (37) and (38), see Equation (50).

3.4. Analytical Solution for the Damping Rate of the Surface Kink Mode in the Alfvén Continuum

Considering the Alfvén resonance, we have a dispersion relation from Equation (22)

$$\rho_i(\omega^2 - \omega_{Ai}^2) - \rho_e(\omega^2 - \omega_{Ae}^2)\frac{k_i}{k_e}Q_m + \frac{i\pi m^2}{\rho_A|\Delta_A|r_A^2}\rho_i\rho_e(\omega^2 - \omega_{Ai}^2)(\omega^2 - \omega_{Ae}^2)\frac{G_m}{k_e} = 0, \tag{39}$$

and the analytical formula for γ_m is given as

$$\gamma_{Am} = -\frac{\frac{\pi m^2\rho_e}{k_e\rho_A\,|\Delta_A|\,r_A^2}(\omega_r^2 - \omega_{Ai}^2)(\omega_r^2 - \omega_{Ae}^2)G_m}{2\omega_r\left[1 - \chi\left(\frac{k_i}{k_e}\right)Q_m\right] - \omega_r\chi T_m}, \tag{40}$$

where only the numerator is slightly changed when compared with Equation (28). From Equation (39), it is inferred that no resonant absorption in the Alfvén continuum occurs for the sausage waves since the imaginary part becomes zero when $m = 0$.

For the surface kink mode ($m = 1$) in the Alfvén continuum, we obtain

$$\gamma_{A1} = -\frac{\pi\rho_e}{k_e\rho_A|\Delta_A|r_A^2}\frac{(\omega_r^2-\omega_{Ai}^2)(\omega_r^2-\omega_{Ae}^2)G_1}{2\omega_r\left[1-\chi\left(\frac{k_i}{k_e}\right)Q_1\right]-\omega_r\chi T_1}. \tag{41}$$

3.5. Long Wavelength Limit ($m = 1$)

In the limit $k_iR(k_eR) \ll 1$, γ_{A1} reduces to (see Appendix B), by using the asymptotic expansion of Q_1, G_1, P_1, and S_1 (Equations (67)–(70)),

$$\gamma_{A1} = \frac{\pi\rho_e R}{\rho_A|\Delta_A|r_A^2} \times \frac{(\omega_r^2-\omega_{Ai}^2)(\omega_r^2-\omega_{Ae}^2)}{2\omega_r\left[1+\chi\left(1+\frac{k_i^2R^2}{4}\right)\right]-\omega_r\chi T_1}, \tag{42}$$

where

$$T_1 = -\omega_r^2(\omega_r^2-\omega_{Ae}^2)\left\{\frac{(\omega_r^2-2\omega_{Ci}^2)(k_iR)^2}{2(\omega_r^2-\omega_{si}^2)(\omega_r^2-\omega_{Ai}^2)(\omega_r^2-\omega_{Ci}^2)} + \frac{(\omega_r^2-2\omega_{Ce}^2)[-(k_iR)^2/4+(1+3\ln(k_eR))(k_eR)^2]}{(\omega_r^2-\omega_{se}^2)(\omega_r^2-\omega_{Ae}^2)(\omega_r^2-\omega_{Ce}^2)}\right\}. \tag{43}$$

For $k_zR \ll 1$ and $\omega_r \approx \omega_{Ci}$ (using Equations (12)–(14)), Equation (42) is reduced to

$$\gamma_{A1} = \frac{\pi\chi R}{|\Delta_A|r_i^2}\frac{(\omega_{Ci}^2-\omega_{Ai}^2)(\omega_{Ci}^2-\omega_{Ae}^2)}{2\omega_{Ci}\left[1+\frac{\omega_{Ci}^2\omega_{Ai}^2}{\omega_{si}^2(\omega_{Ci}^2-\omega_{Ae}^2)}\right]-\chi\omega_{Ci}T_1}, \tag{44}$$

where

$$T_1 = -\frac{8\omega_{si}^2\omega_{Ai}^2(\omega_{Ci}^2-\omega_{Ae}^2)}{\omega_{Ci}^6k_z^2R^2}\left(\frac{\omega_{Ci}^2\omega_{Ai}^2}{\chi\omega_{si}^2(\omega_{Ci}^2-\omega_{Ae}^2)}-1\right)^2, \tag{45}$$

where we have left the most dominant term (see Appendix B). Due to the factor $1/(k_zR)^2$ in the denominator of Equation (45), we may further reduce Equation (44) into

$$\gamma_{A1} \approx -\frac{\pi}{8|\Delta_A|R}\frac{\omega_{Ci}^7k_z^2R^2}{\omega_{si}^4}\left(\frac{\omega_{Ci}^2\omega_{Ai}^2}{\chi\omega_{si}^2(\omega_{Ci}^2-\omega_{Ae}^2)}-1\right)^{-2}, \tag{46}$$

where we have used $r_i \approx R$. For the photospheric (magnetic pore) conditions (ω_{Ae}, $\omega_{Ce} \simeq 0$), we obtain

$$\gamma_{A1} = -\frac{\pi}{8|\Delta_A|R}\frac{\omega_{Ci}^7k_z^2R^2}{\omega_{si}^4}\left(\frac{\omega_{Ai}^2}{\chi\omega_{si}^2}-1\right)^{-2} = -\frac{\pi}{8|\Delta_A|R}\frac{\chi^2\omega_{Ci}^7k_z^2R^2}{(\omega_{Ai}^2-\chi\omega_{si}^2)^2}. \tag{47}$$

For two slow surface modes in the long wavelength limit, comparison of the above three resonant absorption effects leads to the conclusion that the wave damping due to the Alfvén resonance is stronger than that due to the slow resonance:

$$\frac{\gamma_{A1}}{\gamma_{c0}} = -\frac{3}{16\chi}\frac{|\Delta_c|}{|\Delta_A|}\frac{\omega_{Ai}^{10}}{\omega_{si}^2\omega_{Ci}^4(\omega_{Ai}^2-\chi\omega_{si}^2)^2}\frac{1}{k_z^2R^2\ln^3(k_zR)}, \tag{48}$$

$$\frac{\gamma_{A1}}{\gamma_{c1}} = \frac{|\Delta_c|}{|\Delta_A|}\frac{\omega_{Ai}^4}{\omega_{Ci}^4k_z^2R^2}, \tag{49}$$

$$\frac{\gamma_{c0}}{\gamma_{c1}} = -\frac{16\chi}{3}\frac{\omega_{si}^2(\omega_{Ai}^2-\chi\omega_{si}^2)^2\ln^3(k_zR)}{\omega_{Ai}^6}. \tag{50}$$

These formulas provide a relative strength among three different resonant absorptions for the surface sausage and kink modes in the long wavelength limit such that at $k_zR \approx 0$ the damping due to the Alfvén resonance is much stronger than due to the slow resonance and, for the slow resonance, the resonant absorption for the slow surface sausage mode is stronger than for the slow surface kink mode. These features are proven in Figure 11. In the figure, it is also shown that there is a crossover between two curves for slow resonance and the curve for Alfvén resonance, after which the resonant damping of the slow resonance dominates over that of the Alfvén resonance.

Caution is needed for using these formulae in the long wavelength limit, given their limited validity range, as we showed in Figure 5 in Yu et al. (2017).

4. Linear Profiles for the Density and Pressure

In this paper, we consider a linear profile for the density and pressure (or equivalently squared magnetic field) in the nonuniform layer. For the linear density profile, we define $\rho = \rho_i + (\rho_e - \rho_i)(r - r_i)/(r_e - r_i)$. The position of resonance where resonant absorption occurs depends on the wave frequency in the slow or Alfvén continuum ($v = v_{C,A}$): $r = r(v)$. We introduce a new variable δ such that $r = r_i + \delta(r_e - r_i)$ in the transitional layers, where $0 \leqslant \delta \leqslant 1$. That is $\delta = (r - r_i)/(r_e - r_i)$. This makes it more convenient to derive the formula for the position of resonance in terms of resonance (cusp or Alfvén) frequency. Then we can represent the density ρ as a function of δ such that $\rho = \rho_i + \delta(\rho_e - \rho_i)$. Assuming also a linear variation of pressure p, we may set $p = p_i + \delta(p_e - p_i)$ as like ρ, then it is straightforward to show that B^2 also has a similar relation $B^2 = B_i^2 + \delta(B_e^2 - B_i^2)$. In this way, the variables v_s, v_A, and v_C can be represented as (see Appendix C)

$$v_s = v_{si}\frac{\sqrt{1+\delta(\chi v_{sei}^2-1)}}{\sqrt{1+\delta(\chi-1)}}, \tag{51}$$

$$v_A = v_{Ai}\frac{\sqrt{1+\delta(\chi v_{Aei}^2-1)}}{\sqrt{1+\delta(\chi-1)}}, \tag{52}$$

$$v_C^2 = \frac{v_{si}^2v_{Ai}^2}{v_{si}^2[1+\delta(\chi v_{sei}^2-1)]+v_{Ai}^2[1+\delta(\chi v_{Aei}^2-1)]} \times \frac{[1+\delta(\chi v_{sei}^2-1)][1+\delta(\chi v_{Aei}^2-1)]}{1+\delta(\chi-1)}, \tag{53}$$

where $v_{sei}^2 = v_{se}^2/v_{si}^2$ and $v_{Aei}^2 = v_{Ae}^2/v_{Ai}^2$.

In Figure 3, we plot v_s, v_A, and v_C under the magnetic pore condition, where $v_{Ae} = 0\ \mathrm{km\ s^{-1}}$, $v_{Ai} = 12\ \mathrm{km\ s^{-1}}$,

$v_{se} = 11.5$ km s^{-1}, and $v_{si} = 7$ km s^{-1}. The parameters inside the magnetic pore are taken from Grant et al. (2015) and those outside the magnetic pore are typical values of the photosphere. Note that the cusp speed v_C covers some range of slow body and slow surface modes, so resonant absorption can occur for both slow surface and slow body sausage modes in the slow continuum and for slow body kink modes in the Alfvén continuum.

Since the value of δ is not obtainable from observations with the current resolution of the instruments, we need to find the expression for δ in terms of v_C or v_A (see, e.g., Soler et al. 2009). From Equation (53), we derive the quadratic formula for $\delta(=\delta_c)$ with respect to v_C

$$A\delta^2 + B\delta + C = 0, \tag{54}$$

where

$$A = 1 + \frac{v_C^2}{v_{Ci}^2}(\chi - 1) + \chi\left[\frac{v_C^2}{v_{Ci}^2} - (v_{sei}^2 + v_{Aei}^2)\right] - \chi^2\left(\frac{v_C^2}{v_{Ci}^2} - v_{sei}^2 v_{Aei}^2\right), \tag{55}$$

$$B = 2\left(\frac{v_C^2}{v_{Ci}^2} - 1\right) - \chi\left[\frac{v_C^2}{v_{Ci}^2}\left(1 + \frac{v_{se}^2 + v_{Ae}^2}{v_{si}^2 + v_{Ai}^2}\right) - (v_{sei}^2 + v_{Aei}^2)\right], \tag{56}$$

$$C = 1 - \frac{v_C^2}{v_{Ci}^2}, \tag{57}$$

which yields two solutions (see the curve v_C in Figure 3):

$$\delta_{c1} = -\frac{B}{2A} + \frac{\sqrt{B^2 - 4AC}}{2A} \ (0 < \delta_{c1} \leqslant \delta_m), \tag{58}$$

$$\delta_{c2} = -\frac{B}{2A} - \frac{\sqrt{B^2 - 4AC}}{2A} \ (\delta_m < \delta_{c2} \leqslant 1), \tag{59}$$

where δ_m is the value of δ when v has a maximum value v_{Cm} (here $\delta_m \approx 0.26$, $v_{Cm} \approx 0.93 v_{si}$ for the magnetic pore condition). When $0 < \delta(=\delta_{c1}) < \delta_m$ v_C is from v_{Ci} to v_{Cm}. When $\delta_m < \delta(=\delta_{c2}) < 1$, v_C is from v_{Cm} to v_{Ce}.

As a result, $\triangle_c$ is given as (see Appendix C)

$$\triangle_c = -\left(\frac{\omega_C^2}{l}\right)\left\{\frac{(\chi v_{sei}^2 - 1)}{1 + \delta_c(\chi v_{sei}^2 - 1)} - \frac{(\chi - 1)}{1 + \delta_c(\chi - 1)} + \frac{(\chi v_{Aei}^2 - 1)}{1 + \delta_c(\chi v_{Aei}^2 - 1)} - \frac{v_{si}^2(\chi v_{sei}^2 - 1) + v_{Ai}^2(\chi v_{Aei}^2 - 1)}{v_{si}^2[1 + \delta_c(\chi v_{sei}^2 - 1)] + v_{Ai}^2[1 + \delta_c(\chi v_{Aei}^2 - 1)]}\right\}, \tag{60}$$

where $\omega_C = \omega_C(\delta = \delta_c)$ and $\delta_c = \delta_{c1}, \delta_{c2}$

For the slow surface sausage mode to resonantly damp, $v(=\omega_r/k_z)$ should be below v_{Ci}, which means that only δ_{c2} satisfies this condition. For the slow body sausage modes to undergo resonant damping, both solutions are needed because for $v_{Ci} < v < v_{Cm}$ resonant absorption occurs at two resonance positions δ_{c1} and δ_{c2}.

From Equation (52), we derive a formula for $\delta(=\delta_a)$ with respect to v_A

$$\delta_a = \frac{1 - (v_A/v_{Ai})^2}{1 - (v_A/v_{Ai})^2 + \chi[(v_A/v_{Ai})^2 - v_{Aei}]}. \tag{61}$$

Then $\triangle_A$ becomes (see Appendix C)

$$\triangle_A = -\left(\frac{\omega_A^2}{l}\right)\left\{\frac{\chi v_{Aei}^2 - 1}{1 + \delta_a(\chi v_{Aei}^2 - 1)} - \frac{\chi - 1}{1 + \delta_a(\chi - 1)}\right\}, \tag{62}$$

where $\omega_A = \omega_A(\delta = \delta_a)$. The resonant position r_A can be written in terms of δ_a as $r_A = R + l(\delta_a - 0.5)$, which we use in the calculation of Equations (41) and (44).

5. Results

We have considered the linear density and linear pressure (squared magnetic field) profiles for the transitional layer given in Section 4. We first deal with resonant absorption in the slow continuum. In Figure 4, by using an analytical formula, Equation (32), we plot the damping rate $-\gamma_{c0}/\omega_r$ for the slow surface sausage mode as a function of (a) $k_z R$ and (b) v/v_{si} when $l/R = 0.1$. The parameters for each phase speed are described in the caption. The damping rate $-\gamma_{c0}/\omega_r$ increases as $k_z R$ increases and as v/v_{si} decreases. If we take $k_z R = 5$, $-\gamma_{c0}/\omega_r \approx 0.023$, then the ratio of damping time to the period τ_D/T is $(1/|\gamma_{c0}|)/(2\pi/\omega_r) = 1/(2\pi|\gamma_{c0}|/\omega_r) \approx 6.825$, which is a bit larger than the typical value for the resonant damping of the kink mode (2–4). This result could mean, contrary to previous interpretation, that the slow continuum may play a key role in the decay of the slow sausage mode and heating the lower chromosphere in certain situations. Although Equation (32) is valid for a small damping ($|\gamma_m| \ll \omega_r$), it is necessary to check its validity range by comparing with the numerical solution of Equation (24).

We compare the above analytical result with the numerical result. To obtain the analytical solution (Equation (32)), we previously put $\omega_r(v)$ equal to the eigenfrequency of the undamped situation (i.e., $l/R = 0$). But, in practice, the inclusion of the transitional layer (resonant layer) modifies both the real part ω_r and the imaginary part γ_{c0} of the wave frequency. In Figure 5(a), we show the l/R-dependent behavior of ω_r as a function of $k_z R$. As l/R increases, ω_r shifts upward into a higher frequency, crossing over the frequency corresponding to $\omega_{Ci}(v_{Ci})$ at some value of $k_z R$. By crossing over it, it gets into the regime of the body modes and Equation (24) is no longer valid. We need to solve the connection formula for the body modes here. For the body mode, multiple eigenmodes and, as a result, multiple different damping rates for each $k_z R$ are obtainable. We plot one solution curve for each l/R in the frequency regime of the body mode (above the line v_{Ci}) in the figure, by connecting the surface mode.

In Figure 5(b), we plot the damping rate $-\gamma_{c0}/\omega_r$ for $l/R = 0.1, 0.2, 0.3, 0.4$. For each value of l, the numerical solution has a local peak at a certain value of $k_z R$, while the analytical solution looks like a quadratic function of $k_z R$. A similar behavior of having a local maximum was found for the kink mode considering a linear density profile (Soler et al. 2013). As the value of l/R becomes smaller, the peak position moves to higher values of $k_z R$ along with the increment of the maximum value of the damping rate. When $l/R = 0.1$, the maximum value of the damping rate is

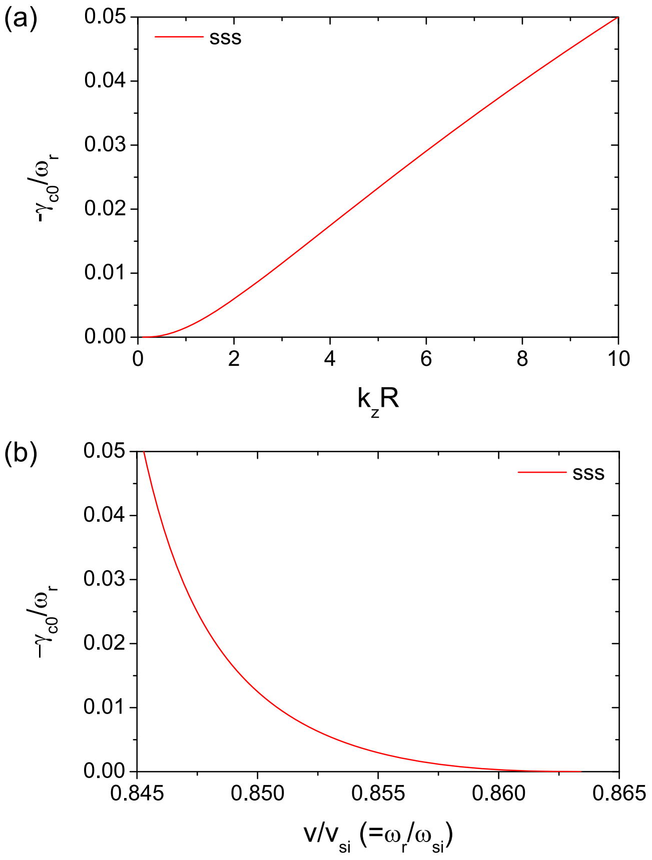

Figure 4. Analytical formula for the damping rate $-\gamma_{c0}/\omega_r$, Equation (32), vs. (a) k_zR and (b) $v/v_{si}(=\omega/\omega_{si})$ for the slow sausage surface mode (sss), where $l/R = 0.1$, $v_{Ae} = 0$ km s^{-1}, $v_{Ai} = 12$ km s^{-1}, $v_{se} = 11.5$ km s^{-1}, $v_{si} = 7$ km s^{-1}, $\beta_i = (2/\gamma)(v_{si}/v_{Ai})^2 = 0.4083$, and $\beta_e = (2/\gamma)(v_{se}/v_{Ae})^2 = \infty$. The linear profiles for the density and pressure considered in Section 4 are used.

$-\gamma_0/\omega_r \approx 0.01$, which results in $\tau_D/T \approx 14.11$. Although this ratio is large compared to the typical values (2–4) observed for the kink modes and the corresponding value of the analytical solution, it is not ignorable as previously expected and could be effective for wave damping. When the curve of phase speed crosses over the line v_{Ci}, the curve and the relevant damping rate correspond to body modes. As we have explained in Figure 5(a), in the body mode range of $v_{Ci} < v < v_{si}$, multiple damping rates are obtainable. In the figure, we plot only one solution curve of the body modes, which connects the surface sausage mode below the line v_{Ci}. We apply the same procedure to slow body kink modes.

In Figure 5(c), we plot the ratio of the damping time to the period $\tau_D/T\,(=1/(2\pi(-\gamma_{c0}/\omega_r)))$ for $l/R = 0.1, 0.2, 0.3, 0.4$. It has an inverse relation with the damping rate by its definition. It has a dip where the damping is most strong, which moves to the left as l/R increases. As l/R decreases, the minimum value (value at the dip) of τ_D/T gradually approaches about 10.5.

From the seismological point of view, the thickness of the transitional layer can be inferred from the damping time of the excited wave modes. So, the relation between the damping rate (time) and the thickness is of interest. In Figure 6, we see the l/R dependence of (a) the phase speed (eigenfrequency) v/v_{si}, (b) damping rate $-\gamma_{c0}/\omega_r$, and (c) the ratio of the damping time to the period τ_D/T by using Equation (24). When k_zR is small, the frequency monotonically increases, but for $k_zR > 1$ it

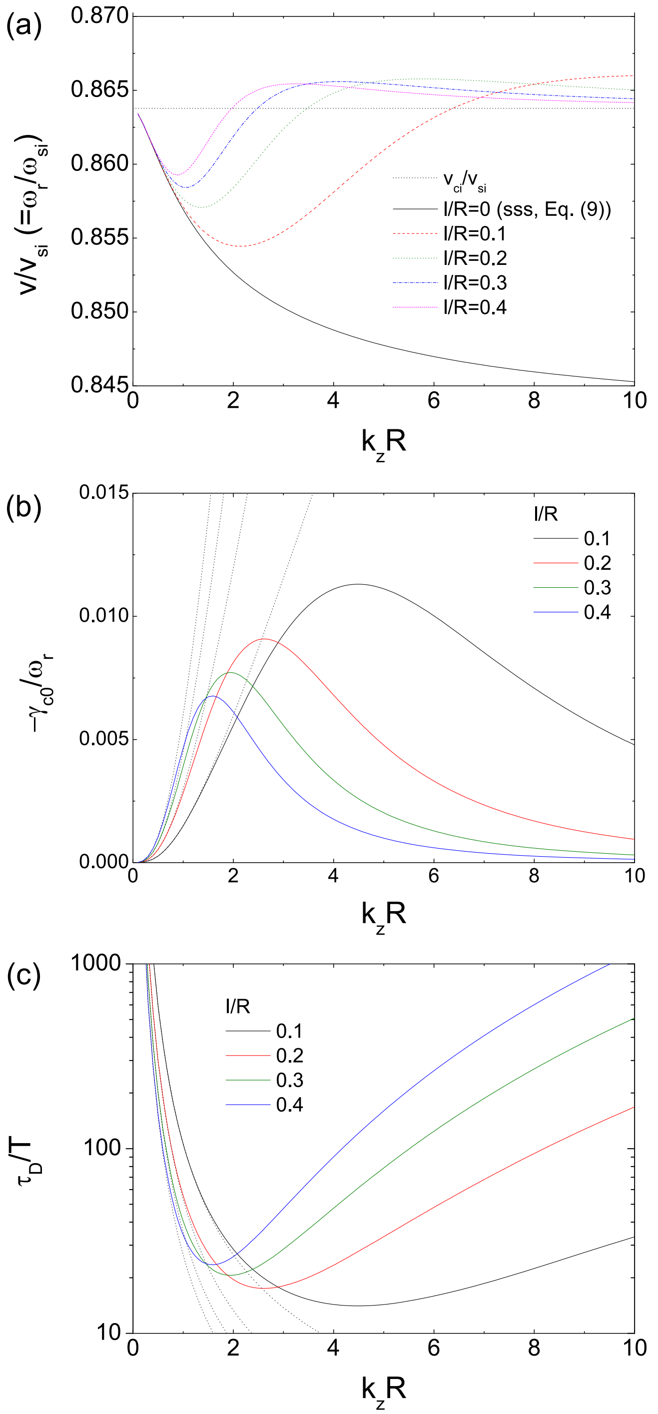

Figure 5. (a) The phase speed of the slow surface sausage (sss) mode v/v_{si} vs. k_zR. We compare the solution of Equation (9) (solid line) without an inhomogeneous (transitional) layer with the solutions (dashed, dotted, dashed–dotted, and short-dashed lines) of Equation (24) with the transitional layer introduced in Section 4 when $l/R = 0.1, 0.2, 0.3, 0.4$. The other parameters are the same as in previous figures. Each solution curve above the dotted line (v_{Ci}) corresponds to that of body modes. (b) The damping rate $-\gamma_{c0}/\omega_r$ vs. k_zR corresponding to curves in (a). The analytical approximations (dotted lines), Equation (32), are compared to the numerical solutions (solid lines), Equation (24), for $m = 0$. As l/R increases, the curve of the numerical solution shifts to the left while decreasing. The analytical and numerical solutions for each l/R converge when the value of k_zR approaches zero. (c) The ratio of the damping time to the period τ_D/T (logarithmic scale) vs. k_zR. The position of the dip shifts to the right as l/R decreases and its value tends to approximately approach 10.5.

reaches a local peak and then decreases. For large k_zR, the wave frequency approaches $\omega_{Ci}(v_{Ci})$ as l/R increases. The damping rate is in proportion to l/R when k_zR is small. As k_zR increases, the curve tends to have a local peak. The curve becomes sharper with an increment as k_zR increases and the position of the peak shifts to smaller values of k_zR. This represents that the damping is efficient when k_zR is large and l/R is small. The ratio of damping time to the period reveals the opposite behavior to the damping rate as inferred from its definition. From the figure, it is anticipated that τ_D/T could reach around 10 when the magnetic flux tube is very thin. From the behavior of the l/R-dependent damping rate, resonant absorption and the relevant damping of the slow surface sausage mode in the slow continuum would become significant for thinner transitional layers and for waves with small longitudinal wavelength.

We point out that for phase speeds larger than v_{Ci}, which corresponds to the slow body sausage mode, one solution curve connected to the slow surface sausage mode is plotted for each k_zR, where one resonance point ($\delta = \delta_{c2}$) is considered as in the previous figure. We postpone a detailed study on resonant absorption of slow body modes to the future.

Together with the slow surface sausage mode, the slow surface kink mode can undergo resonant absorption in the slow continuum. In Figure 7, we plot the k_zR dependence of the (a) phase speed, (b) damping rate, and (c) ratio of the damping time to the period for $l/R = 0.1$, 0.2, 0.3, 0.4. The deviation of the phase speed and damping rate from the $l/R = 0$ case appears very similar to the case of the slow surface sausage mode. As l/R increases, the phase speed shifts upward crossing the line v_{Ci} entering into the body mode range. The curve of the damping rate decreases as l/R increases and the peak position moves to smaller k_zR values. Soler et al. (2009) obtained a similar curve for the kink modes in solar filaments/prominence. They showed that for $l/R = 0.2$, $\tau_D/T \approx 1000$ as a minimum value, while our result gives that it is about 19. The effect of the slow resonance on the wave damping is significant under photospheric conditions.

In Figure 8, we plot the l/R dependence of the (a) phase speed, (b) damping rate, and (c) ratio of the damping time to the period for the slow surface kink mode when $k_zR = 0.5$, 1, 2, 4, 8. All the features explained for Figure 6 can apply here. The difference of resonant absorption in the slow continuum between the slow surface mode with $m = 0$ and one with $m = 1$ is small (see Figure 11). Such as in the previous two figures for the slow surface sausage modes, in Figures 7 and 8, the damping rate (time) for one of the slow body kink modes is plotted by connecting the slow surface kink mode when the phase speed is above v_{Ci}.

While the slow surface sausage mode has no resonant absorption in the Alfvén continuum since there is no azimuthal magnetic field in the equilibrium, we have two resonant absorptions for slow and fast surface kink modes in the Alfvén continuum. In Figure 9, we show the (a) phase speed v/v_{si}, (b) damping rate $-\gamma_{c1}/\omega_r$, and (c) ratio of the damping time to the period τ_D/T for the slow surface kink mode as a function of k_zR when $l/R = 0.1$, 0.2, 0.3, 0.4. We use Equation (39) for numerical results and Equation (41) for analytical results. The wave frequency has little dependence on the l/R, slightly shifting upward as l/R increases. When $l/R = 0.1$, it is hard to distinguish from the original dispersion curve. The damping rate shows an increasing and then decreasing behavior having a local maximum (peak) at $k_zR \approx 2$, similar to the behavior of the slow surface sausage mode. As l/R increases, the damping rate increases in the whole range of k_zR and the peak position shifts gradually to the right in the figure. It is worth noting that the analytic results are very close to the numerical result, which means that the analytic formula, Equation (41), is a valid approximation for the resonant damping of the slow surface kink mode in the Alfvén continuum in the whole range of k_zR. The deviation of the numerical result from the analytical one becomes larger as l/R increases. To compare with the slow surface sausage mode, the effect of the resonant damping on the slow surface kink mode looks much weaker than that of the

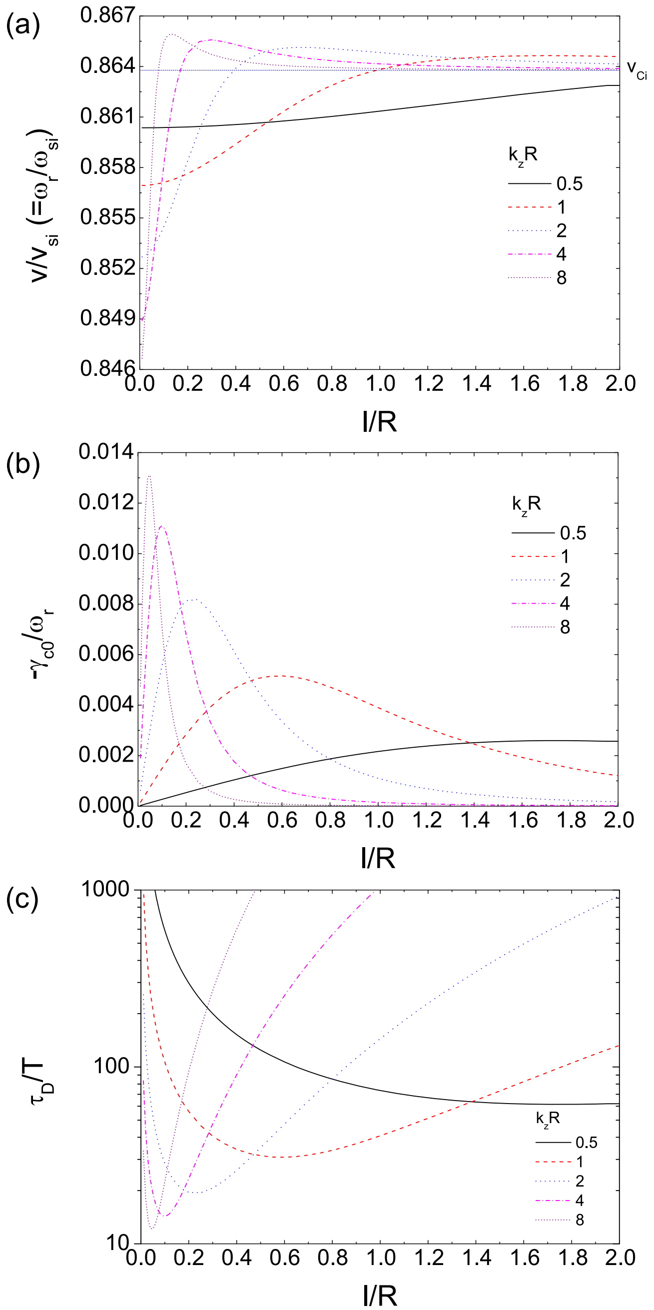

Figure 6. (a) v/v_{si} vs. l/R for the slow surface sausage (sss) mode when $k_zR = 0.5$, 1, 2, 4, 8. The other parameters are the same as in previous figures. Each solution curve above the dotted line (v_{Ci}) corresponds to that of body modes. For larger k_zR, as l/R increases the wave frequency approaches $\omega_{Ci}(v_{Ci})$. (b) The damping rate $-\gamma_{c0}/\omega_r$ vs. l/R. Each curve has a local peak whose position shifts to a smaller l/R as k_zR increases, resulting in a higher damping rate. (c) τ_D/T (logarithmic scale) vs. l/R. For a sufficiently large value of k_zR, it has a local dip, which moves to smaller l/R as k_zR increases.

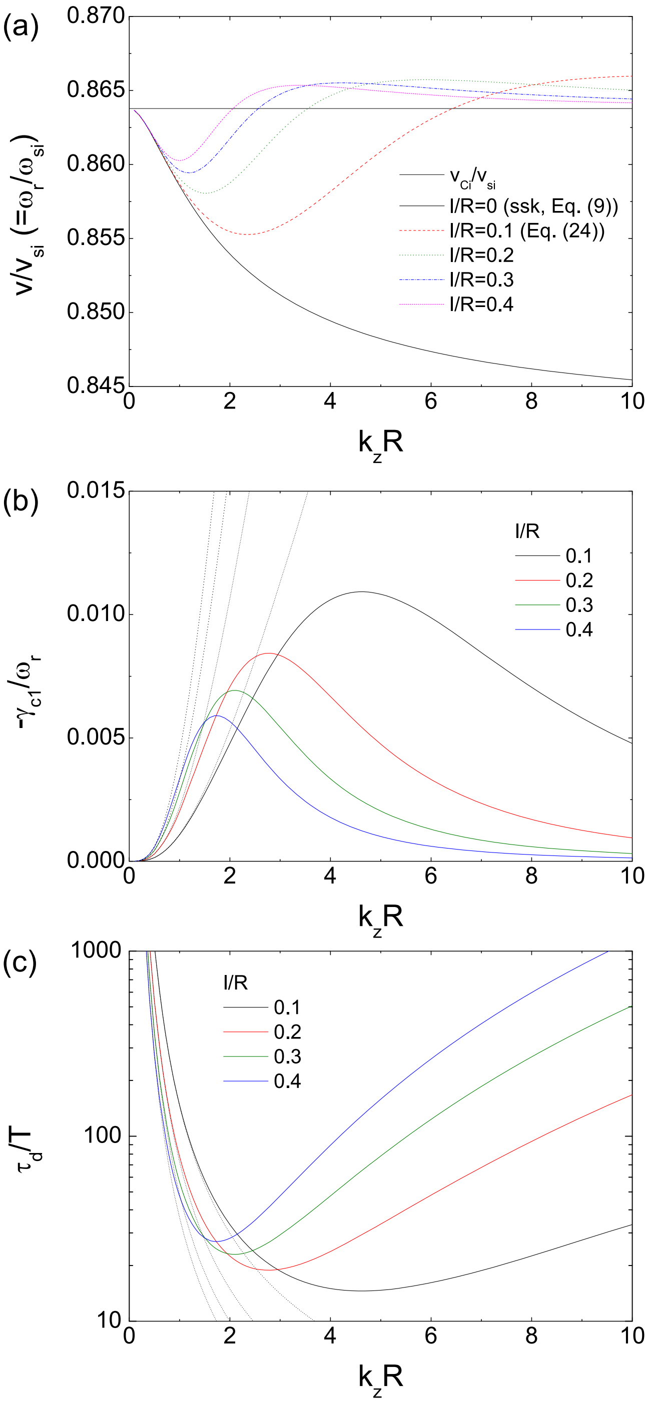

Figure 7. (a) The phase speed of the slow surface kink (ssk) mode v/v_{si} vs. k_zR. We compare the solution of Equation (9) (solid line) without an inhomogeneous (transitional) layer with the solutions (dashed, dotted, dashed–dotted, and short-dashed lines) of Equation (24) with the transitional layer introduced in Section 4 when $l/R = 0.1,\ 0.2,\ 0.3,\ 0.4$. The other parameters are the same as in previous figures. The solution curve above the dotted line (v_{Ci}) corresponds to that of slow body kink modes. (b) The damping rate $-\gamma_{c1}/\omega_r$ vs. k_zR. The analytical approximations (dotted lines), Equation (33), are compared to the numerical solutions (solid lines), Equation (24), for $m = 1$. As l/R increases, the curve of the numerical solution shifts to the left while decreasing. The analytical and numerical solutions for each l/R converge when the value of k_zR approaches zero. (c) The ratio of damping time to period τ_D/T (logarithmic scale) vs. k_zR. The features in (a)–(c) are very similar to those of the slow surface sausage mode (Figure 5).

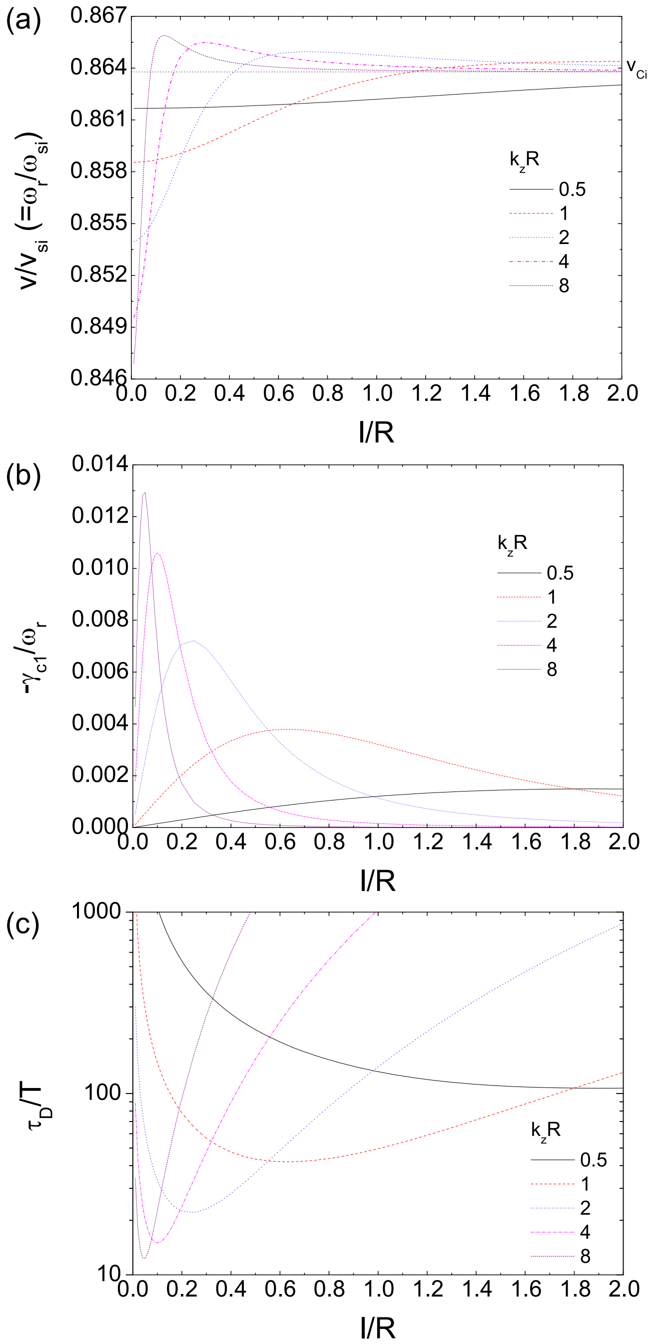

Figure 8. (a) The phase speed of the slow surface kink (ssk) mode v/v_{si} vs. l/R. We show the l/r-dependent variation of the wave frequency when $k_zR = 0.5,\ 1,\ 2,\ 4,\ 8$. The solution curve above the dotted line (v_{Ci}) corresponds to that of slow body kink modes. For larger k_zR, as l/R increases the wave frequency approaches $\omega_{Ci}(v_{Ci})$. (b) The damping rate $-\gamma_{c1}/\omega_r$ vs. l/R. Each curve has a local peak whose position shifts to a smaller l/R as k_zR increases, resulting in a higher damping rate. (c) The ratio of damping time to the period τ_D/T (logarithmic scale) vs. l/R. For a sufficiently large value of k_zR, it has a local dip that moves to smaller l/R as k_zR increases. The features in (a)–(c) are very similar to those of the slow surface sausage mode (Figure 6).

slow surface sausage mode for small l/R (see Figure 11 for more detail). The damping time over the period also appears to have a dip that goes down as l/R increases, which is opposite to the two cases for the slow resonance. On the contrary, its behavior for the prominence reported by Soler et al. (2009) is very different, where for $l/R = 0.2$ the damping time over the period was shown to not change from about 5 until k_zR increases up to 0.1, after which it increases rapidly as k_zR increases. When $l/R = 0.2$, we have $\tau_D/T \approx 100$ as a minimum value. It was shown by Soler et al. (2009) that in

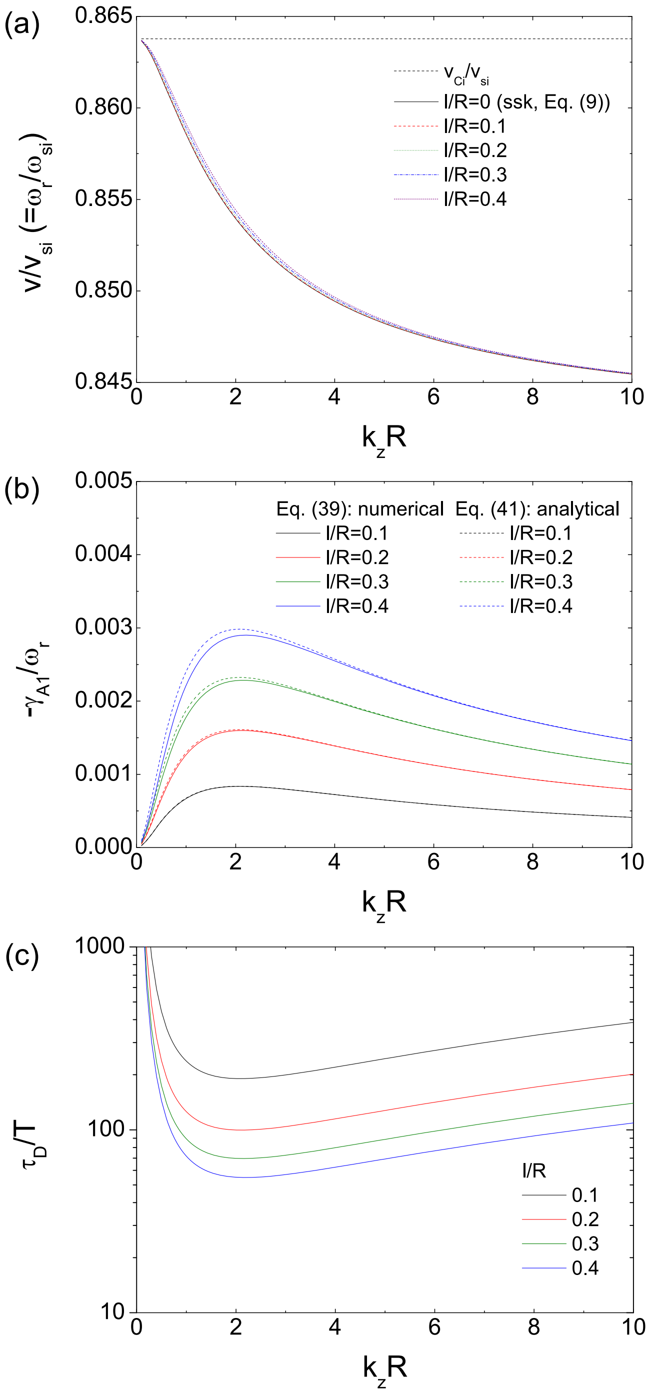

Figure 9. (a) The phase speed v/v_{si} of the slow surface kink (ssk) mode vs. k_zR. We compare the solution of Equation (9) (solid black line) without an inhomogeneous (transitional) layer with the solutions (dashed, dotted, dashed–dotted, short-dashed lines) of Equation (39) with the transitional layer introduced in Section 4 where $l/R = 0.1, 0.2, 0.3, 0.4$. The other parameters are the same as in previous figures. The wave frequency shifts upwards with few changes as l/R increases, which is different from the sausage mode. (b) The damping rate $-\gamma_{A1}/\omega_r$ of the slow surface kink mode in the Alfvén continuum vs. k_zR. The analytical approximations (Equation (41), dashed lines) are compared to the numerical solutions (Equation (39), solid lines) for $m = 1$. As l/R increases, the damping rate increases over the whole range of k_zR and the peak position moves to the right. The analytical solutions are consistent with the numerical solutions where the deviation, which is still small, increases as l/R increases. (c) The ratio of the damping time to the period τ_D/T (logarithmic scale) vs. l/R: numerical calculations, Equation (39).

the solar filaments/prominences, the wave damping due to Alfvén resonance is stronger than due to the slow resonance, which is reversed in the photospheric environment.

In Figure 10, we show the l/R-dependent behavior of the slow surface kink mode by numerical calculation (Equation (39) for $m = 1$) when $k_zR = 0.5, 1, 2, 3, 4, 6, 8, 10$. It is found that (a) the phase speed has a small monotonic increment for each k_zR, similar to k_zR dependence. In (b) the damping rate is shown to increase as a function of l/R. The damping rate first increases as k_zR increases up to about 3 and then decreases again, in the whole range of l/R. It has a maximum value at $k_zR \approx 3$. As a result, (c) the ratio of the damping time to the period τ_D/T has a minimum at $k_zR \approx 3$. For the slow surface kink mode, it is expected that resonant absorption is strongest when $k_zR \approx 3$ and l/R is large. The value of τ_D/T reaches about 21.6 when $k_zR = 3$ and $l/R = 2$.

In our model configuration, the slow and Alfvén continua do not overlap in the transitional layer. Hence when a wave is damped, it is either in the slow continuum or Alfvén continuum. There is no combination of the two resonant damping effects. If the two resonances overlap in the transitional layer, a combined effect could change the results for the slow surface kink mode, requiring further investigations.

We can think of the situation that two slow surface modes are excited simultaneously with the same amplitude since two modes are in the same frequency range. In Figure 11, we compare the three resonance effects: slow resonance on the slow surface sausage and slow surface kink modes and Alfvén resonance on the slow surface kink mode when $l/R = 0.1$. The two slow surface modes undergo a similar damping process in the slow resonance, while the effect of resonant damping for slow surface kink mode in the Alfvén continuum is quite small. As predicted from Equations (48) and (49), when $k_zR \ll 1$, the damping effect in the Alfvén continuum is bigger than the damping effect in the slow continuum. As k_zR increases, the role of the two resonant effects is reversed and the difference increases until the damping rate in the slow continuum reaches a maximum. There is a crossover at $k_zR \approx 0.6$ and $k_zR \approx 0.78$. This feature maintains regardless of the value of l/R. If two slow modes are excited concurrently with a small longitudinal wavelength ($k_zR > 1$), the slow surface kink mode would survive much longer than the slow surface sausage mode when ignoring other dissipation effects. As inferred from Equation (50), it is also shown in the figure that the slow surface sausage mode is more easily damped than the slow surface kink mode in the slow continuum in the long wavelength limit.

Considering resonant absorption of the fast surface kink mode in the Alfvén continuum, we find that the absorption behavior is different from that of the slow surface kink mode. It is shown in Figure 12(a) that the phase speed shifts downward as l/R increases, where $l/R = 0.1, 0.2, 0.3, 0.4$, which is opposite to the case of the slow surface kink mode. The value of the shift is small, but increases gradually as l/R increases. In Figure 12(b), the damping rate approaches its maximum as k_zR goes to zero and monotonically decreases as k_zR becomes large from zero. This feature can be inferred from the fact that the denominator of Equation (41) is proportional to $k_z^2R^2$ when k_zR is small. The resonance effect for the fast surface kink mode is much bigger in comparison with the slow surface kink mode, leading to a strong wave damping such as under coronal conditions. The difference between analytical and numerical results grows proportionally to l/R, similar to the case of the slow surface kink mode. In Figure 12(c), the ratio of the damping time to the period is shown to increase as k_zR increases and as l/R increases. The damping effect due to resonant absorption is most strong when $k_zR \approx 0$ and l/R is large.

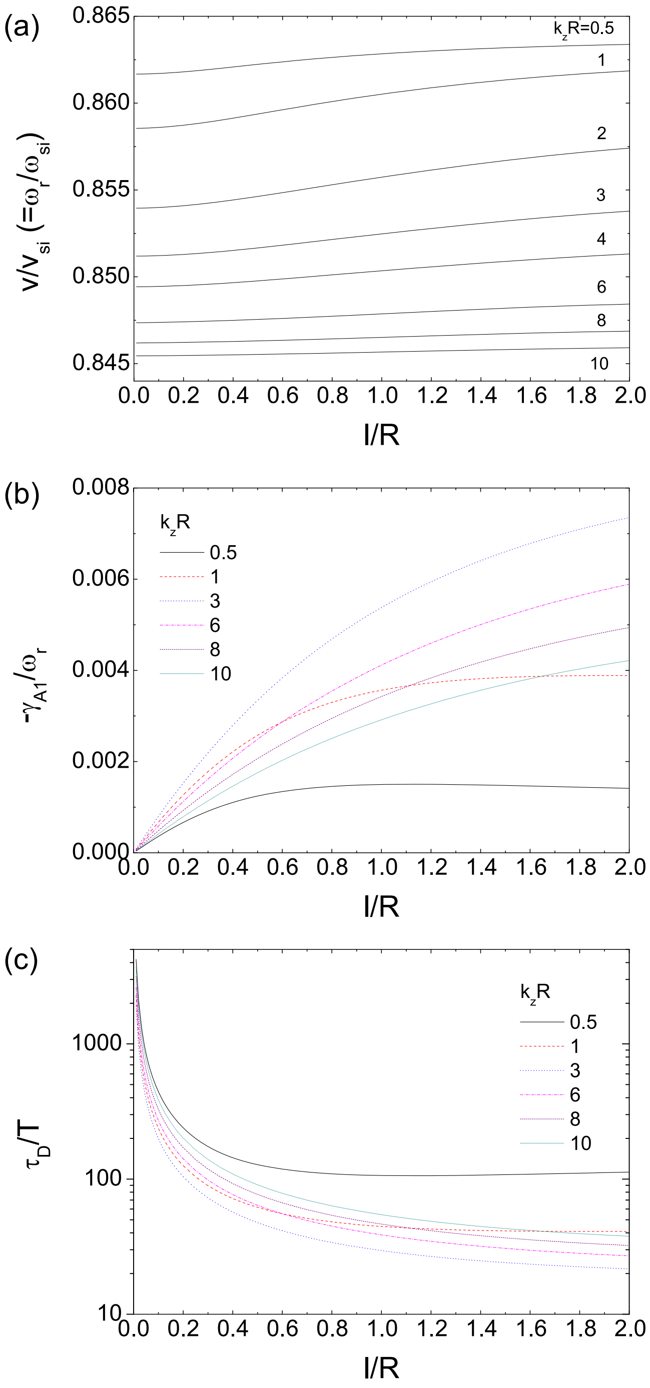

Figure 10. Numerical calculations of resonant absorption for the slow surface kink (ssk) mode in the Alfvén continuum: Equation (39). (a) v/v_{si} vs. l/R when $k_zR = 0.5$, 1, 2, 3, 4, 6, 8, 10. As l/R increases the frequency shifts gradually upward. The l/R-dependent frequency shift is small, as for the k_zR dependence. (b) $-\gamma_{A1}/\omega_r$ vs. l/R when $k_zR = 0.5$, 1, 3, 6, 8, 10 (numerical calculation, Equation (39)). Each curve increases monotonically as l/R increases. For $k_zR < 3$, the damping rate increases gradually in the whole range of l/R and after $k_zR \approx 3$ it decreases. (c) τ_D/T (logarithmic scale) vs. l/R. The damping effect becomes significant as l/R increases, while being most strong at $k_zR \approx 3$.

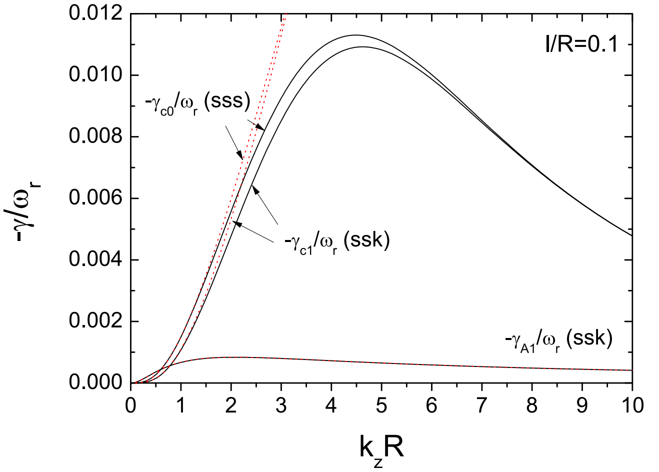

Figure 11. Comparison of the damping rate $-\gamma_{c0}/\omega_r$, $-\gamma_{c1}/\omega_r$, and $-\gamma_{A1}/\omega_r$ as a function of k_zR when $l/R = 0.1$. Solid black lines represent numerical results while dotted red lines represent analytical results. For a small k_zR, both analytical approximation and numerical result show that the resonant damping of the slow surface kink (ssk) mode in the Alfvén continuum is stronger than that of the slow surface sausage (sss) and kink (ssk) modes in the slow resonance. There is a crossover between the damping rate due to the Alfvén resonance and one due to slow resonance at certain values of k_zR. This feature is valid regardless of the value of l/R. The analytical calculations of slow surface sausage and kink modes undergoing the slow resonance converge to the numerical results when k_zR goes to zero. On the contrary, the analytical solution of the slow surface kink mode undergoing the Alfvén resonance is almost the same as the numerical result.

In Figure 13, we present the l/R dependence of the (a) phase speed, (b) damping rate, and (c) ratio of the damping time to the period when $k_zR = 0.5$, 1, 2, 4, 6, 8, 10. The phase speed decreases as l/R increases where the degree of change is big when k_zR is small and becomes small as k_zR increases. It also shows small deviations when l/R is small, which means that the phase speed (or wave frequency) does not vary much for thin transitional layers. The behavior of the damping rate has a similar dependence on l/R with the slow surface kink mode. There is no nonmonotonic behavior with respect to k_zR, which appears for the ssk mode. It is remarkable that the ratio of the damping time to the period can reach below 1 when k_zR is small and l/R is sufficiently large, which means that resonant absorption of the fast surface kink mode is very strong even under photospheric conditions, although the result is based on the restricted assumption of thin transitional layers. The change of resonant absorption becomes small when $l/R > 1$.

6. Conclusion

In a recent paper, we derived a general analytical formula (Equation (28)) for the damping rate of the slow surface sausage mode in the slow continuum by considering the thin boundary (TB) approximation (Yu et al. 2017). In this paper, we have focused on resonant absorption both in the slow and Alfvén continua under photospheric conditions, considering linear density and pressure (or squared magnetic field) profiles in the transitional layers. In order to study resonant absorption in the Alfvén continuum, we have applied the same procedure to obtain Equation (28) and derived another analytical formula, Equation (40).

In Yu et al. (2017), we have applied Equation (28) to the observational rapid damping of the slow surface sausage mode in Grant et al. (2015). For the conventional magnetic pore $R \approx 0.5$–3 Mm and $k_z = 2\pi/\lambda_z = 2\pi/4400$ km, which yields $k_zR \approx 0.7$–4.3. For $k_zR = 4.3$ and $l/R = 0.5$, our previous study based on the assumption of a linear cusp speed yields $-\gamma_{c0}/\omega_r = 0.0089$ and $\tau_D/T \approx 17.9$. This value is reduced by a factor of about 10 by using the linear density and linear pressure profiles in the transitional layer considered in this paper. This result implies that resonant absorption in the slow

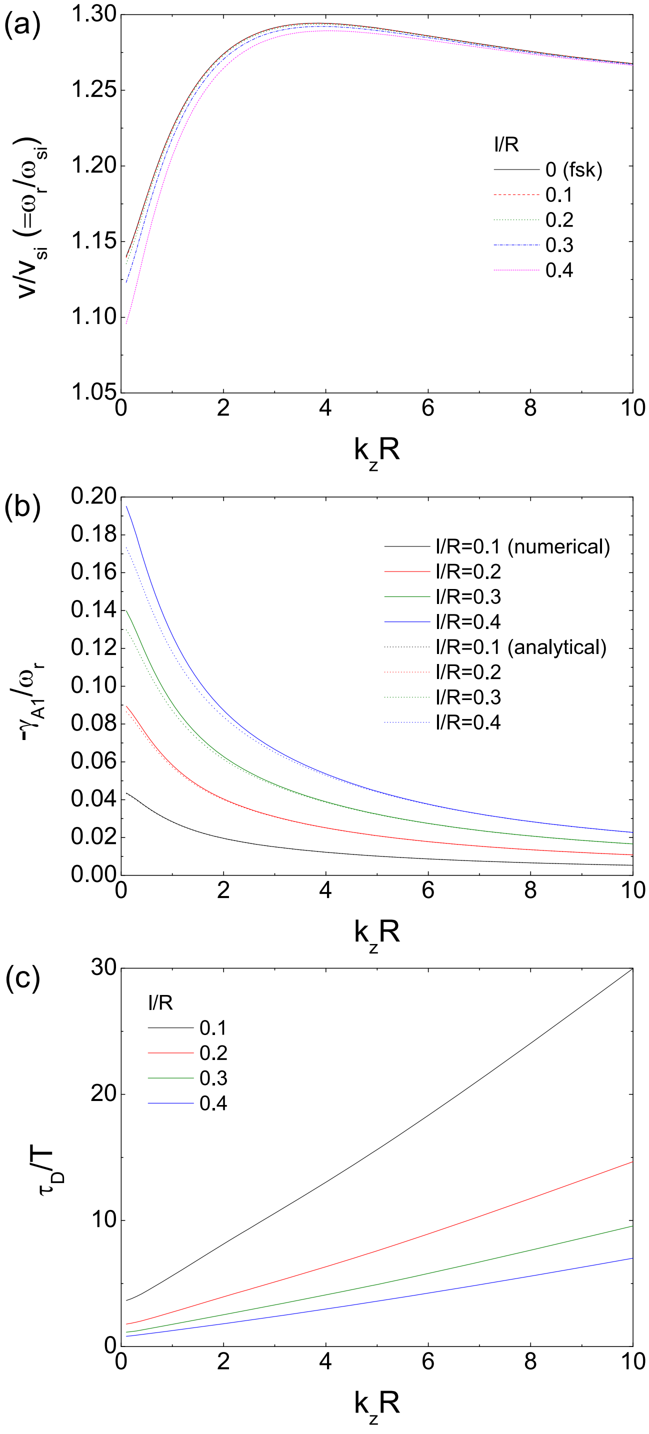

Figure 12. Numerical calculations of resonant absorption for the fast surface kink (fsk) mode in the Alfvén continuum: Equation (39). (a) The phase speed v/v_{si} of the fast surface kink (fsk) mode vs. k_zR. We compare the solution of Equation (9) (fsk, solid black line) without an inhomogeneous (transitional) layer with the solutions (dashed, dotted, dashed–dotted, short-dahsed lines) of Equation (39) with the transitional layer introduced in Section 4, where $l/R = 0.1, 0.2, 0.3, 0.4$. The wave frequency shifts downwards with small changes as l/R increases. The amount of shift becomes larger as k_zR approaches zero. These curves are convergent when k_zR goes to infinity. (b) The damping rate $-\gamma_{A1}/\omega_r$ of the fast surface kink mode in the Alfvén continuum vs. k_zR. As l/R increases the damping rate increases over the whole range of k_zR. Solid lines are obtained from Equation (39) and dotted lines from Equation (41). (c) The ratio of the damping time to the period τ_D/T vs. l/R: numerical calculations, Equation (39).

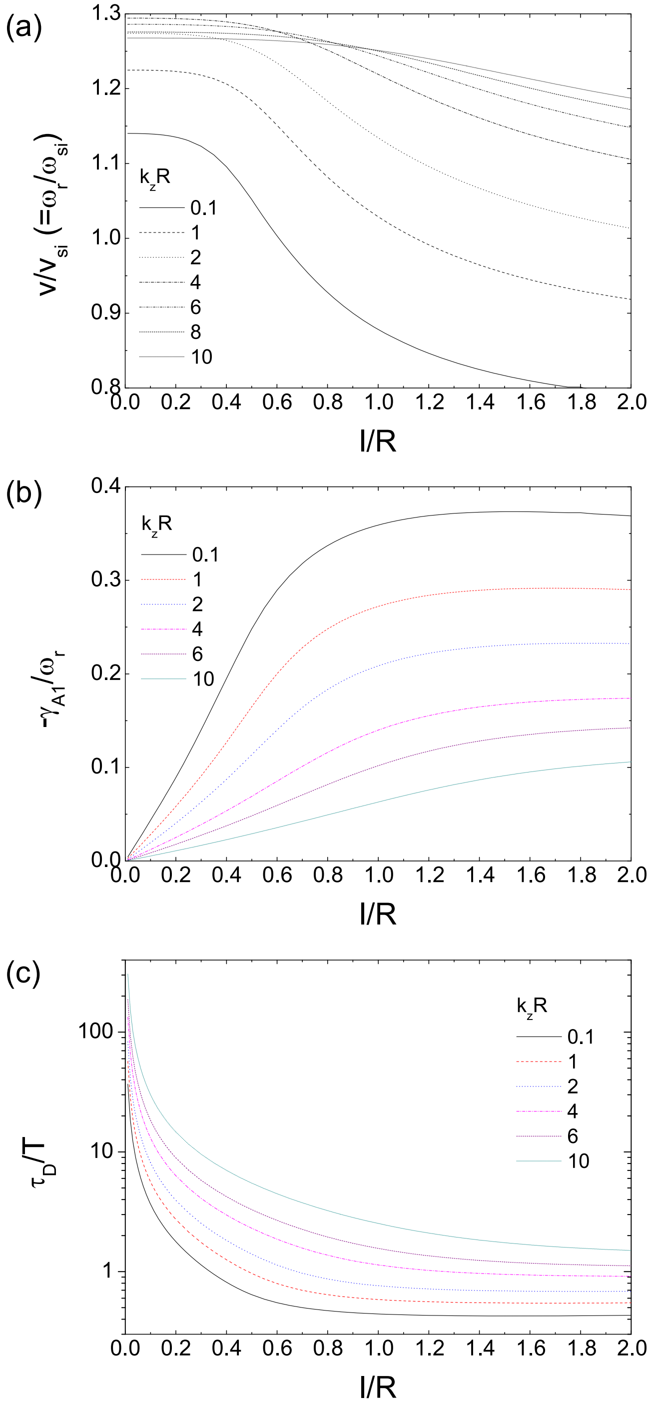

Figure 13. Numerical calculations for the fast surface kink (fsk) mode: Equation (39). (a) v/v_{si} vs. l/R. We show the l/r-dependent variation of the wave frequency when $k_zR = 0.5$, 1, 2, 4, 6, 8, 10. The other parameters are the same as in previous figures. As l/R increases, the frequency shifts gradually downward. The l/R-dependent frequency shift is big for small k_zR and decreases as k_zR increases. (b) $-\gamma_{A1}/\omega_r$ vs. l/R when $k_zR = 0.5$, 1, 2, 4, 6, 10. Each curve increases monotonically as l/R increases reaching a plateau for large l/R. (c) τ_D/T (logarithmic scale) vs. l/R. The damping effect becomes significant for smaller k_zR and larger l/R.

continuum could be efficient as a wave damping mechanism in the lower solar atmosphere. Another important point to mention is that resonant absorption is sensitive to the profiles of the physical quantities in the nonuniform layers. These analytical approximations predict that the damping rate increases as l/R and k_zR increase, but the numerical calculations show that it has a maximum value depending on both l/R and k_zR. The peak position shifts toward smaller k_zR values, while decreasing its strength as l/R increases. For example, when $l/R = 0.1$, $-\gamma_{c0}/\omega_r = 0.01128$, then $\tau_D/T \approx 14.11$. Although this value seems quite big in comparison with the strong (rapid) damping, $\tau_D/T \simeq 2 - 4$, of the fast kink modes in the Alfvén continuum under coronal conditions, the resonant damping due to slow resonance could still be an efficient wave damping mechanism. Although we found that resonant absorption in the slow continuum is an efficient mechanism, this effect is too weak to explain the extremely rapid damping of the slow surface sausage mode observed by Grant et al. (2015). Other damping mechanisms, like, e.g., thermal conduction, are needed.

The slow surface kink mode can resonantly damp both in the slow and Alfvén continua. Its behavior in the slow continuum is very similar to the above features of the slow surface sausage mode. Therefore, a similar wave damping due to resonant absorption in the slow continuum is expected for these two slow surface modes ($m = 0, 1$).

For resonant absorption in the Alfvén continuum, it is found that the resonant damping manifests in a different way for each slow and fast surface kink mode. For the slow surface kink mode, the damping rate draws a curve as a function of k_zR, having a local maximum (peak) at a certain k_zR and is proportional to l/R regardless of the value of k_zR. The l/R dependence of the damping time looks like following a power law when l/R is small. The damping effect is most strong when $k_zR \approx 3$ and $l/R = 2$. When $k_zR = 3$ and $l/R = 2$, $-\gamma_{A1}/\omega_r \approx 0.0735$, which gives $\tau_D/T \approx 21.6$. For the fast surface kink mode, the damping rate is a monotonically decreasing function of k_zR and a monotonically increasing function of l/R. It becomes stronger as k_zR goes to zero and l/R increases. It is shown that the damping of the fast surface kink mode due to the resonance in the Alfvén continuum could be very rapid in the photosphere as much as in the corona. For these kink modes, contrary to the slow surface sausage mode, the analytical approximations agree well with the numerical calculations.

Comparing resonant absorption of two slow surface modes, we could say that the strength of resonant absorption in the slow resonance is higher than that in the Alfvén resonance except when k_zR is very small. This relation is reversed as k_zR increases. For a small value of k_zR (long wavelength limit), we have derived analytical approximate formulas for three kinds of resonant absorption and compared their relative strengths (Equations (48)–(50)), which are well consistent with the numerical results.

Our study has dealt with only linear profiles for the density and pressure leaving a possibility of a higher damping rate for other certain profiles, for example, as shown by Soler et al. (2013) that linear, parabolic, and sinusoidal density profiles induce different behavior of damping rate for the kink mode under coronal conditions.

There is indeed a warning of using the obtained results for the thick transitional layers, as, e.g., Van Doorsselaere et al. (2004) pointed out that the thin tube thin boundary approximation induces significant deviation from exact numerical solutions up to 25% for the coronal loop oscillations. Because we considered only an inhomogeneity in the radial direction, the stratification in the longitudinal direction (e.g., Andries et al. 2005; Arregui et al. 2005; Dymova & Ruderman 2006) or azimuthal direction may as well affect the resonant absorption behavior. Since the magnetic fluxes in the lower solar atmosphere are highly structured, the extension of the existing analytic approach of one-dimensional resonant absorption to two or three dimensions is critical. Another subject we would mention is the resonant behavior of the body modes for $m = 0, 1$, which we leave as a future study.

T.V.D. thanks the support from the Odysseus type II funding (FWO-Vlaanderen), IAP P7/08 CHARM (Belspo), GOA-2015-014 (KU Leuven), and European Research Council (ERC) under the European Union's Horizon 2020 research and innovation programme (grant agreement No. 724326).

Appendix A
Surface Mode

For the surface mode with $m = 1$, we have

$$G_1 = \frac{K_1(k_eR)}{K_1'(k_eR)} = \frac{-2K_1}{K_0 + K_2}, \tag{63}$$

$$\begin{aligned} Q_1 &= \frac{I_1'(k_iR)K_1(k_eR)}{I_1(k_iR)K_1'(k_eR)} = \left(\frac{I_0 + I_2}{2I_1}\right)\left(\frac{-2K_1}{K_0 + K_2}\right) \\ &= -\frac{K_1(I_0 + I_2)}{I_1(K_0 + K_2)}, \end{aligned} \tag{64}$$

$$\begin{aligned} P_1 &= \left(\frac{I_1''}{I_1} - \frac{I_1'^2}{I_1^2}\right)\frac{K_1}{K_1'} \\ &= \left(\frac{3I_1 + I_3}{4I_1} - \frac{(I_0 + I_2)^2}{4I_1^2}\right)\frac{-2K_1}{K_0 + K_2}, \end{aligned} \tag{65}$$

$$\begin{aligned} S_1 &= \left(1 - \frac{K_1''K_1}{K_1'^2}\right)\frac{I_1'}{I_1} \\ &= \left[1 - \frac{(3K_1 + K_3)K_1}{(K_0 + K_2)^2}\right]\frac{I_0 + I_2}{2I_1}. \end{aligned} \tag{66}$$

For the case $k_iR(k_eR) < 1$ (first order approximation), we derive

$$\begin{aligned} G_1 &\approx \frac{\frac{1}{k_eR} - \frac{1}{4} + \frac{1}{2}[\ln(\frac{k_eR}{2}) + \gamma_e]}{-\frac{1}{(k_eR)^2} + \frac{1}{4} + \frac{1}{2}[\ln(\frac{k_eR}{2}) + \gamma_e]} \\ &\approx -k_eR, \end{aligned} \tag{67}$$

$$Q_1 \approx \left(\frac{1}{k_iR} + \frac{k_iR}{4}\right)(-k_eR) = -\left(\frac{k_e}{k_i} + \frac{k_ik_eR^2}{4}\right), \tag{68}$$

$$\begin{aligned} P_1 &\approx -k_eR\left(\frac{I_1''}{I_1} - \frac{I_1''^2}{I_1^2}\right) \\ &\approx -k_eR\left[\frac{\frac{3}{2}k_iR}{2k_iR} - \left(\frac{1}{k_iR} + \frac{k_iR}{4}\right)^2\right] \\ &= -k_eR\left[\frac{3}{4} - \left(\frac{1}{k_iR} + \frac{k_iR}{4}\right)^2\right] \\ &\approx -k_eR\left(\frac{1}{4} - \frac{1}{(k_iR)^2}\right), \end{aligned} \tag{69}$$

$$\begin{aligned}
S_1 &= \left(1 - \frac{K_1''K_1}{K_1''^2}\right)\frac{I_1'}{I_1} \approx \frac{1}{k_iR}\left(1 - \frac{K_1''}{K_1''^2}\right)\\
&= \frac{1}{k_iR}\left\{1 - \frac{\left(\frac{2}{(k_eR)^3} + \frac{1}{2k_eR} + \frac{k_eR[-5 + 12(\ln(k_eR/2) + \gamma_e)]}{32}\right)}{\left(-\frac{1}{(k_eR)^2} + \frac{1 + 2(\ln(k_eR/2) + \gamma_e)}{4}\right)^2}\right.\\
&\quad \left.\times\left(\frac{1}{k_eR} + \frac{k_eR[-1 + 2(\ln(k_eR/2) + \gamma_e)]}{4}\right)\right\}\\
&\approx \frac{1}{k_iR}\left\{1 - \frac{\left(2 + \frac{(k_eR)^2}{2})(1 + \frac{(k_eR)^2}{4}(-1 + 2f)\right)}{1 - \frac{(k_eR)^2}{2}(1 + 2f)}\right\}\\
&\approx \frac{1}{k_iR}\left[1 - \frac{2 + f(k_eR)^2}{1 - \frac{(k_eR)^2}{2}(1 + 2f)}\right]\\
&\approx \frac{1}{k_iR}[1 - (2 + (k_eR)^2(1 + 3f))]\\
&= -\frac{1 + [1 + 3(\ln(k_eR/2) + \gamma_e)](k_eR)^2}{k_iR}\\
&\approx -\frac{1 + [1 + 3\ln(k_eR)](k_eR)^2}{k_iR},
\end{aligned} \tag{70}$$

where γ_e is the Euler's constant and, for S_1, $f = \ln(k_eR/2) + \gamma_e$ is used.

For the $m = 0$ case, see Appendix A in Yu et al. (2017).

Appendix B
Damping Rate for the Surface Mode

Here we briefly summarize the procedure to obtain the damping rate $-\gamma_m/\omega_r$ (see Yu et al. 2017). In order to calculate γ_m, we need to derive the expression for $\partial D_{mr}/\partial\omega$, where ω should be in the slow (cusp) or Alfvén continuum. We have

$$\begin{aligned}
\frac{\partial D_{mr}}{\partial\omega} &= 2\rho_i\omega - 2\omega\rho_e\left(\frac{k_i}{k_e}\right)Q_m\\
&\quad - \rho_e(\omega^2 - \omega_{Ae}^2)\left(\frac{1}{k_e}\frac{dk_i}{d\omega} - \frac{k_i}{k_e^2}\frac{dk_e}{d\omega}\right)Q_m\\
&\quad - \rho_e(\omega^2 - \omega_{Ae}^2)\left(\frac{k_i}{k_e}\right)\frac{dQ_m}{d\omega}.
\end{aligned} \tag{71}$$

For $dk_i/d\omega$ and $dk_e/d\omega$, we obtain

$$\frac{dk_i}{d\omega} = -\frac{\omega^3}{v_{si}^2 + v_{Ai}^2}\frac{(\omega^2 - 2\omega_{Ci}^2)}{(\omega^2 - \omega_{Ci}^2)^2k_i}, \tag{72}$$

$$\frac{dk_e}{d\omega} = -\frac{\omega^3}{v_{se}^2 + v_{Ae}^2}\frac{(\omega^2 - 2\omega_{Ce}^2)}{(\omega^2 - \omega_{Ce}^2)^2k_e}. \tag{73}$$

For $dQ_m/d\omega$, we obtain

$$\begin{aligned}
\frac{dQ_m}{d\omega} &= R\left(\frac{I_m''}{I_m} - \frac{I_m'^2}{I_m^2}\right)\frac{K_0}{K_0'}\frac{dk_i}{d\omega}\\
&\quad + R\left(1 - \frac{K_m''K_m}{K_m'^2}\right)\frac{I_m'}{I_m}\frac{dk_e}{d\omega},
\end{aligned} \tag{74}$$

where the prime means the derivative with respect to the entire argument.

By means of Equations (72) and (73), Equation (74) becomes

$$\begin{aligned}
\frac{dQ_m}{d\omega} &= \frac{k_iRP_m\omega^3(\omega^2 - 2\omega_{Ci}^2)}{(\omega^2 - \omega_{si}^2)(\omega^2 - \omega_{Ai}^2)(\omega^2 - \omega_{Ci}^2)}\\
&\quad + \frac{k_eRS_m\omega^3(\omega^2 - 2\omega_{Ce}^2)}{(\omega^2 - \omega_{se}^2)(\omega^2 - \omega_{Ae}^2)(\omega^2 - \omega_{Ce}^2)},
\end{aligned} \tag{75}$$

where P_m and S_m are

$$P_m = \left(\frac{I_m''}{I_m} - \frac{I_m'^2}{I_m^2}\right)\frac{K_m}{K_m'}, \tag{76}$$

$$S_m = \left(1 - \frac{K_m''K_m}{K_m'^2}\right)\frac{I_m'}{I_m}. \tag{77}$$

Using Equations (72), (73), and (75), we have for $\partial D_{mr}/\partial\omega (= dD_{mr}/d\omega)$

$$\begin{aligned}
\frac{dD_{mr}}{d\omega} &= 2\rho_i\omega - 2\omega\rho_e\left(\frac{k_i}{k_e}\right)Q_m\\
&\quad - \rho_e\omega^3(\omega^2 - \omega_{Ae}^2)\left(\frac{k_i}{k_e}\right)\\
&\quad \times \frac{(\omega^2 - 2\omega_{Ci}^2)[Q_m + k_iRP_m]}{(\omega^2 - \omega_{si}^2)(\omega^2 - \omega_{Ai}^2)(\omega^2 - \omega_{Ci}^2)}\\
&\quad + \rho_e\omega^3(\omega^2 - \omega_{Ae}^2)\left(\frac{k_i}{k_e}\right)\\
&\quad \times \frac{(\omega^2 - 2\omega_{Ce}^2)[Q_m - k_eRS_m]}{(\omega^2 - \omega_{se}^2)(\omega^2 - \omega_{Ae}^2)(\omega^2 - \omega_{Ce}^2)}.
\end{aligned} \tag{78}$$

Then the imaginary term γ_m for the surface wave in the slow (cusp) continuum is

$$\begin{aligned}
\gamma_m &= -\frac{D_{mi}}{\frac{\partial D_{mr}}{\partial\omega}}\Big|_{\omega=\omega_r}\\
&= -\frac{\frac{\pi\rho_ek_z^2}{k_e\rho_c\,|\triangle_c|}\left(\frac{v_{sc}^2}{v_{sc}^2 + v_{Ac}^2}\right)^2(\omega_r^2 - \omega_{Ai}^2)(\omega_r^2 - \omega_{Ae}^2)G_m}{2\omega_r\left[1 - \chi\left(\frac{k_i}{k_e}\right)Q_m\right] - \omega_r\chi T_m},
\end{aligned} \tag{79}$$

where

$$\begin{aligned}
T_m &= \omega_r^2(\omega_r^2 - \omega_{Ae}^2)\left(\frac{k_i}{k_e}\right)\left\{\frac{(\omega_r^2 - 2\omega_{Ci}^2)[Q_m + k_iRP_m]}{(\omega_r^2 - \omega_{si}^2)(\omega_r^2 - \omega_{Ai}^2)(\omega_r^2 - \omega_{Ci}^2)}\right.\\
&\quad \left. - \frac{(\omega_r^2 - 2\omega_{Ce}^2)[Q_m - k_eRS_m]}{(\omega_r^2 - \omega_{se}^2)(\omega_r^2 - \omega_{Ae}^2)(\omega_r^2 - \omega_{Ce}^2)}\right\}.
\end{aligned} \tag{80}$$

Likewise, for the surface wave in the Alfvén continuum, we obtain

$$\gamma_m = -\frac{\frac{\pi\rho_em^2}{k_e\rho_A\,|\triangle_A|\,r_A^2}(\omega_r^2 - \omega_{Ai}^2)(\omega_r^2 - \omega_{Ae}^2)G_m}{2\omega_r\left[1 - \chi\left(\frac{k_i}{k_e}\right)Q_m\right] - \omega_r\chi T_m}. \tag{81}$$

In the limit $k_iR(k_eR) \ll 1$, T_1 becomes with the help of Equations (67)–(70)

$$T_1 = -\omega_r^2(\omega_r^2 - \omega_{Ae}^2)\left\{\frac{(\omega_r^2 - 2\omega_{Ci}^2)(k_iR)^2}{2(\omega_r^2 - \omega_{si}^2)(\omega_r^2 - \omega_{Ai}^2)(\omega_r^2 - \omega_{Ci}^2)} + \frac{(\omega_r^2 - 2\omega_{Ce}^2)[-(k_iR)^2/4 + (1 + 3\ln(k_eR))(k_eR)^2]}{(\omega_r^2 - \omega_{se}^2)(\omega_r^2 - \omega_{Ae}^2)(\omega_r^2 - \omega_{Ce}^2)}\right\}. \tag{82}$$

For the slow surface kink mode with $k_zR \ll 1$ ($\omega_r \approx \omega_{Ci}$), by the aid of Equations (12)–(14), Equation (82) reduces to

$$\begin{aligned} T_1 = &-\omega_{Ci}^2(\omega_{Ci}^2 - \omega_{Ae}^2)\left\{\frac{-\omega_{Ci}^2(k_iR)^2}{2(\omega_{Ci}^2 - \omega_{si}^2)(\omega_{Ci}^2 - \omega_{Ai}^2)\alpha}\right. \\ &\left. + \frac{(\omega_{Ci}^2 - 2\omega_{Ce}^2)[-(k_iR)^2/4 + (1 + 3\ln(k_eR))(k_eR)^2]}{(\omega_{Ci}^2 - \omega_{se}^2)(\omega_{Ci}^2 - \omega_{Ae}^2)(\omega_{Ci}^2 - \omega_{Ce}^2)}\right\} \\ = &-\omega_{Ci}^2(\omega_{Ci}^2 - \omega_{Ae}^2)\left\{\frac{8\omega_{si}^2\omega_{Ai}^2}{\omega_{Ci}^8k_z^2R^2}\left(\frac{\omega_{Ci}^2\omega_{Ai}^2}{\chi\omega_{si}^2(\omega_{Ci}^2 - \omega_{Ae}^2)} - 1\right)^2\right. \\ &- \frac{1}{(\omega_{Ci}^2 - \omega_{se}^2)(\omega_{Ci}^2 - \omega_{Ae}^2)(\omega_{Ci}^2 - \omega_{Ce}^2)} \\ &\times\left(\frac{\omega_{Ci}^2\omega_{Ai}^2}{\chi\omega_{si}^2(\omega_{Ci}^2 - \omega_{Ae}^2)} - 1\right) \\ &\left. - \frac{(\omega_{Ci}^2 - 2\omega_{Ce}^2)(1 + 3\ln(k_zR))k_z^2R^2}{(\omega_{se}^2 + \omega_{Ae}^2)(\omega_{Ci}^2 - \omega_{Ce}^2)^2}\right\} \\ \approx &-\frac{8\omega_{si}^2\omega_{Ai}^2(\omega_{Ci}^2 - \omega_{Ae}^2)}{\omega_{Ci}^6k_z^2R^2}\left(\frac{\omega_{Ci}^2\omega_{Ai}^2}{\chi\omega_{si}^2(\omega_{Ci}^2 - \omega_{Ae}^2)} - 1\right)^2. \end{aligned} \tag{83}$$

Appendix C
Linear Profiles for the Density, Squared Magnetic Field, and Pressure

For the linear profiles considered in Section 4, the variables v_s, v_A, and v_C in the cusp resonance regime become

$$\begin{aligned} v_s &= \sqrt{\frac{\gamma p_c}{\rho_c}} = \sqrt{\frac{\gamma p_i}{\rho_i}}\sqrt{\frac{p_c}{p_i}}\frac{1}{\sqrt{\rho_c/\rho_i}} \\ &= \frac{v_{si}\sqrt{p_{ci}}}{\sqrt{1 + \delta(\chi - 1)}}, \end{aligned} \tag{84}$$

$$\begin{aligned} v_A &= \frac{B_c}{\sqrt{\mu_0\rho_c}} = \frac{B_i}{\sqrt{\mu_0\rho_i}}\frac{B_c}{B_i}\frac{1}{\sqrt{\rho_c/\rho_i}} \\ &= \frac{v_{Ai}B_{ci}}{\sqrt{1 + \delta(\chi - 1)}}, \end{aligned} \tag{85}$$

$$\begin{aligned} v_C^2 &= \frac{v_s^2v_A^2}{v_s^2 + v_A^2} = \frac{\frac{\gamma p_c}{\rho_c}\frac{B_c}{\sqrt{\mu_0\rho_c}}}{\frac{\gamma p_c}{\rho_c} + \frac{B_c^2}{\mu_0\rho_c}} \\ &= \frac{v_{si}^2v_{Ai}^2}{v_{si}^2p_{ci} + v_{Ai}^2B_{ci}^2}\frac{p_{ci}B_{ci}^2}{1 + \delta(\chi - 1)}, \end{aligned} \tag{86}$$

where $\rho_{ci} = \rho_c/\rho_i$, $p_{ci} = p_c/p_i$, and $B_{ci} = B_c/B_i$. The subscript c represents the value at the resonant position. Assuming a linear variation of the squared magnetic field B^2, we can set $B_c^2 = B_i^2 + \delta(B_e^2 - B_i^2)$ as for ρ_c, then p_c also has a similar relation $p_c = p_i + \delta(p_e - p_i)$ or vice versa. Making use of these variables, Equations (84)–(86) reduce to

$$\begin{aligned} v_s &= \frac{v_{si}\sqrt{p_{ci}}}{\sqrt{1 + \delta(\chi - 1)}} = v_{si}\frac{\sqrt{1 + \delta(p_{ei} - 1)}}{\sqrt{1 + \delta(\chi - 1)}} \\ &= v_{si}\frac{\sqrt{1 + \delta(\chi(v_{se}/v_{si})^2 - 1)}}{\sqrt{1 + \delta(\chi - 1)}} \\ &= v_{si}\frac{\sqrt{1 + \delta(\chi v_{sei}^2 - 1)}}{\sqrt{1 + \delta(\chi - 1)}}, \end{aligned} \tag{87}$$

$$\begin{aligned} v_A &= = \frac{v_{Ai}B_{ci}}{\sqrt{1 + \delta(\chi - 1)}} = v_{Ai}\frac{\sqrt{1 + \delta(B_{ei}^2 - 1)}}{\sqrt{1 + \delta(\chi - 1)}} \\ &= v_{Ai}\frac{\sqrt{1 + \delta(\chi(v_{Ae}/v_{Ai})^2 - 1)}}{\sqrt{1 + \delta(\chi - 1)}} \\ &= v_{Ai}\frac{\sqrt{1 + \delta(\chi v_{Aei}^2 - 1)}}{\sqrt{1 + \delta(\chi - 1)}}, \end{aligned} \tag{88}$$

$$\begin{aligned} v_C^2 &= \frac{v_s^2v_A^2}{v_s^2 + v_A^2} = \frac{v_{si}^2v_{Ai}^2}{v_{si}^2p_{ci} + v_{Ai}^2B_{ci}^2}\frac{p_{ci}B_{ci}^2}{1 + \delta(\chi - 1)} \\ &= \frac{v_{si}^2v_{Ai}^2}{v_{si}^2[1 + \delta(p_{ei} - 1)] + v_{Ai}^2[1 + \delta(B_{ei}^2 - 1)]} \\ &\quad\times\frac{[1 + \delta(p_{ei} - 1)][1 + \delta(B_{ei}^2 - 1)]}{1 + \delta(\chi - 1)}, \\ &= \frac{v_{si}^2v_{Ai}^2}{v_{si}^2[1 + \delta(\chi v_{sei}^2 - 1)] + v_{Ai}^2[1 + \delta(\chi v_{Aei}^2 - 1)]} \\ &\quad\times\frac{[1 + \delta(\chi v_{sei}^2 - 1)][1 + \delta(\chi v_{Aei}^2 - 1)]}{1 + \delta(\chi - 1)}, \end{aligned} \tag{89}$$

where $v_{sei}^2 = v_{se}^2/v_{si}^2$ and $v_{Aei}^2 = v_{Ae}^2/v_{Ai}^2$.

From Equation (86), we derive the formula for $\delta(=\delta_c)$ with respect to v_C:

$$A\delta^2 + B\delta + C = 0, \tag{90}$$

where

$$\begin{aligned} A = 1 &+ \frac{v_C^2}{v_{Ci}^2}(\chi - 1) + \chi\left[\frac{v_C^2}{v_{Ci}^2} - (v_{sei}^2 + v_{Aei}^2)\right] \\ &- \chi^2\left(\frac{v_C^2}{v_{Ci}^2} - v_{sei}^2v_{Aei}^2\right), \end{aligned} \tag{91}$$

$$\begin{aligned} B = 2&\left(\frac{v_C^2}{v_{Ci}^2} - 1\right) - \chi\left[\frac{v_C^2}{v_{Ci}^2}\left(1 + \frac{v_{se}^2 + v_{Ae}^2}{v_{si}^2 + v_{Ai}^2}\right)\right. \\ &\left. - (v_{sei}^2 + v_{Aei}^2)\right], \end{aligned} \tag{92}$$

$$C = 1 - \frac{v_C^2}{v_{Ci}^2}, \tag{93}$$

which leads to two solutions:

$$\delta_{c1} = -\frac{B}{2A} + \frac{\sqrt{B^2 - 4AC}}{2A} \quad (0 < \delta \leqslant \delta_m), \tag{94}$$

$$\delta_{c2} = -\frac{B}{2A} - \frac{\sqrt{B^2 - 4AC}}{2A} \quad (\delta_m \leqslant \delta \leqslant 1), \tag{95}$$

where δ_m is the value of δ when v_C has a maximum value.

For $\triangle_{\mathrm{c}}$, we obtain

$$\begin{aligned}\triangle_c &= d(\omega^2 - \omega_C^2)/dr|_{r=r_c} = -2\omega_{Cc}\frac{d\omega_{Cc}}{dr}\\ &= -2\omega_{Cc}^2\left[\frac{v_{Ac}v_{sc}' + v_{sc}v_{Ac}'}{v_{sc}v_{Ac}} - \frac{v_{sc}v_{sc}' + v_{Ac}v_{Ac}'}{v_{sc}^2 + v_{Ac}^2}\right]\\ &= -\omega_{Cc}^2\left[\frac{p_c'}{p_c} - \frac{\rho_c'}{\rho_c} + 2\frac{B_c'}{B_c} - \frac{v_{sc}^2\left(\frac{P_c'}{P_c}\right) + 2v_{Ac}^2\left(\frac{B_c'}{B_c}\right)}{v_s^2 + v_A^2}\right]\\ &= -\left(\frac{\omega_{Cc}^2}{l}\right)\left\{\frac{(\chi v_{sei}^2 - 1)}{1 + \delta(\chi v_{sei}^2 - 1)} - \frac{(\chi - 1)}{1 + \delta(\chi - 1)}\right.\\ &\quad + \frac{(\chi v_{Aei}^2 - 1)}{1 + \delta(\chi v_{Aei}^2 - 1)}\\ &\quad \left. - \frac{v_{si}^2(\chi v_{sei}^2 - 1) + v_{Ai}^2(\chi v_{Aei}^2 - 1)}{v_{si}^2[1 + \delta(\chi v_{sei}^2 - 1)] + v_{Ai}^2[1 + \delta(\chi v_{Aei}^2 - 1)]}\right\},\end{aligned} \tag{96}$$

where the prime denotes the derivative with respect to r and the subscript c means $r = r_c$.

In the same way, we can derive $\delta(=\delta_a)$ in case of the Alfvén resonance. From Equation (88), we derive the formula for δ with respect to v_A

$$\delta_a = \frac{1 - (v_A/v_{Ai})^2}{1 - (v_A/v_{Ai})^2 + \chi[(v_A/v_{Ai})^2 - v_{Aei}]}. \tag{97}$$

For $\triangle_A$, we obtain

$$\begin{aligned}\triangle_A &= d(\omega^2 - \omega_A^2)/dr|_{r=r_A} = -2\omega_{Aa}\frac{d\omega_{Aa}}{dr}\\ &= -2\omega_{Aa}k_z\left(\frac{B_a}{\sqrt{\mu_0\rho_a}}\right)' = -2\omega_{Aa}^2\left(\frac{B_a'}{B_a} - \frac{1}{2}\frac{\rho_a'}{\rho_a}\right)\\ &= -\left(\frac{\omega_{Aa}^2}{l}\right)\left\{\frac{\chi v_{Aei}^2 - 1}{1 + \delta_a(\chi v_{Aei}^2 - 1)} - \frac{\chi - 1}{1 + \delta_a(\chi - 1)}\right\},\end{aligned} \tag{98}$$

where the subscript a means $r = r_A$ ($\delta = \delta_a$).

ORCID iDs

Dae Jung Yu https://orcid.org/0000-0003-1459-3057
Tom Van Doorsselaere https://orcid.org/0000-0001-9628-4113

References

Andries, J., Goossens, M., Hollweg, J. V., Arregui, I., & Van Doorsselaere, T. 2005, A&A, 430, 1109

Antolin, P., De Moortel, I., Van Doorsselaere, T., & Yokoyama, T. 2017, ApJ, 836, 219

Arregui, I., Andries, J., Van Doorsselaere, T., Goossens, M., & Poedts, S. 2007, A&A, 463, 333

Arregui, I., Van Doorsselaere, T., Andries, J., Goossens, M., & Kimpe, D. 2005, A&A, 441, 361

Aschwanden, M. J., Nightingale, R. W., Andries, J., Goossens, M., & Van Doorsselaere, T. 2003, ApJ, 598, 1375

Bogdan, T. J., Hindman, B. W., Cally, P. S., & Charbonneau, P. 1996, ApJ, 465, 406

Cally, P. S. 2017, MNRAS, 466, 413

De Moortel, I., & Hood, A. W. 2003, A&A, 408, 755

De Moortel, I., & Hood, A. W. 2004, A&A, 415, 705

Dymova, M. V., & Ruderman, M. S. 2006, A&A, 457, 1059

Edwin, P. M., & Roberts, B. 1983, SoPh, 88, 179

Giagkiozis, I., Goossens, M., Verth, G., Fedun, V., & Van Doorsselaere, T. 2016, ApJ, 823, 71

Goossens, M., Andries, J., & Aschwanden, M. J. 2002, A&A, 394, L39

Goossens, M., Arregui, I., Ballester, J. L., & Wang, T. J. 2008, A&A, 484, 851

Goossens, M., Erdélyi, R., & Ruderman, M. S. 2011, SSRv, 158, 289

Goossens, M., Hollweg, J. V., & Sakurai, T. 1992, SoPh, 138, 233

Goossens, M., Soler, R., Arregui, I., & Terradas, J. 2012, ApJ, 760, 98

Grant, S. D. T., Jess, D. B., Moreels, M. G., et al. 2015, ApJ, 806, 132

Heyvaerts, J., & Priest, E. R. 1983, A&A, 117, 220

Hollweg, J. V. 1988, ApJ, 335, 1005

Ionson, J. A. 1978, ApJ, 226, 650

Jess, D. B., Morton, R. J., Verth, G., et al. 2015, SSRv, 190, 103

Jess, D. B., Van Doorsselaere, T., Verth, G., et al. 2017, ApJ, 842, 59

Jess, D. B., & Verth, G. 2016, GMS, 216, 449

Karampelas, K., Van Doorsselaere, T., & Antolin, P. 2017, A&A, 604, A130

Keppens, R. 1996, ApJ, 468, 907

Keppens, R., Bogdan, T. J., & Goossens, M. 1994, ApJ, 436, 372

Khodachenko, M. L., Arber, T. D., Rucker, H. O., & Hanslmeier, A. 2004, A&A, 422, 1073

Krall, N. A., & Trivelpiece, A. W. 1973, Principles of Plasma Physics (Tokyo: McGraw-Hill Kogakusha)

Lou, Y.-Q. 1990, ApJ, 350, 452

Mandal, S., Magyar, N., Yuan, D., Van Doorsselaere, T., & Banerjee, D. 2016, ApJ, 820, 13

McEwan, M. P., Díaz, A. J., & Roberts, B. 2008, A&A, 481, 819

Moreels, M. G., Freij, N., Erdélyi, R., Van Doorsselaere, T., & Verth, G. 2015a, A&A, 579, A73

Moreels, M. G., & Van Doorsselaere, T. 2013, A&A, 551, A137

Moreels, M. G., Van Doorsselaere, T., Grant, S. D. T., Jess, D. B., & Goossens, M. 2015b, A&A, 578, A60

Ofman, L., & Davila, J. M. 1995, JGR, 100, 23427

Okamoto, T. J., Antolin, P., De Pontieu, B., et al. 2015, ApJ, 809, 71

Pascoe, D. J., Wright, A. N., & De Moortel, I. 2010, ApJ, 711, 990

Poedts, S., Goossens, M., & Kerner, W. 1989, SoPh, 123, 83

Poedts, S., Goossens, M., & Kerner, W. 1990, ApJ, 360, 279

Raes, J. O., Van Doorsselaere, T., Baes, M., & Wright, A. N. 2017, A&A, 602, A75

Roberts, B. 2000, SoPh, 193, 139

Rosenthal, C. S. 1990, SoPh, 130, 313

Rosenthal, C. S. 1992, SoPh, 139, 25

Ruderman, M. S. 2009, PhPl, 16, 042109

Ruderman, M. S., & Erdélyi, R. 2009, SSRv, 149, 199

Ruderman, M. S., & Roberts, B. 2002, ApJ, 577, 475

Sakurai, T., Goossens, M., & Hollweg, J. V. 1991, SoPh, 133, 227

Scherrer, B., & McKenzie, D. 2017, ApJ, 837, 24

Soler, R., Goossens, M., Terradas, J., & Oliver, R. 2013, ApJ, 777, 158

Soler, R., Goossens, M., Terradas, J., & Oliver, R. 2014, ApJ, 781, 111

Soler, R., Oliver, R., Ballester, J. L., & Goossens, M. 2009, ApJL, 695, L166

Stenuit, H., Poedts, S., & Goossens, M. 1993, SoPh, 147, 13

Terradas, J., Oliver, R., & Ballester, J. L. 2006a, ApJ, 642, 533

Terradas, J., Oliver, R., & Ballester, J. L. 2006b, ApJL, 650, L91

Van Doorsselaere, T., Andries, J., Poedts, S., & Goossens, M. 2004, ApJ, 606, 1223

Wang, T. 2011, SSRv, 158, 397

Wang, T. J. 2016, GMS, 216, 395

Wang, T. J., Ofman, L., Davila, J. M., & Mariska, J. T. 2009, A&A, 503, L25

Yu, D. J., & Van Doorsselaere, T. 2016, ApJ, 831, 30

Yu, D. J., Van Doorsselaere, T., & Goossens, M. 2017, A&A, 602, A108